IEEE Transactions on Robotics (T-RO) paper presented at
2024 IEEE/RSJ International Conference on Intelligent Robots and Systems (IROS)
October 14-18, 2024. Abu Dhabi, UAE

A Novel Dual-Robot Accurate Calibration Method Using Convex Optimization and Lie Derivative

Cheng Jiang, Wen-long Li, *Member, IEEE*, Wen-pan Li, Dong-fang Wang, Li-jun Zhu, Wei Xu, Huan Zhao, and Han Ding, *Member, IEEE*

***Abstract*—Calibrating unknown transformation relationships is an essential task for multirobot cooperative systems. Traditional linear methods are inadequate to decouple and simultaneously solve the unknown matrices due to their intercoupling. This article proposes a novel dual-robot accurate calibration method that uses convex optimization and Lie derivative to solve the dual-robot calibration problem simultaneously. The key idea is that a convex optimization model based on dual-robot transformation chain is established using Lie representation of special Euclidean group in 3 dimensions [*SE*(3)]. The Jacobian matrix of the established optimization model is explicitly derived using the corresponding Lie derivative of *SE*(3). To balance the influence of the magnitudes of the rotational and translational optimization variables, a weight coefficient is defined. Due to the closure and smoothness of Lie group, the optimization model can be solved simultaneously using Newton-like iterative methods without additional orthogonalization processing. The performance of the proposed method is verified through simulation and actual calibration experiments. The results show that the proposed method outperforms the previous calibration methods in terms of accuracy and stability. The actual experiments are used to compare the proposed method with two existing calibration methods, and the mean measurement error of a certified ceramic sphere is reduced from 0.9205 and 0.5363 to 0.4381 mm, respectively.**

***Index Terms*—AXB = YCZ problem, convex optimization, dual-robot calibration, Lie derivative.**

NOMENCLATURE

$\boldsymbol{A}$	Homogeneous transformation matrix from the end-flange to the base of sensor robot.
$\boldsymbol{B}$	Homogeneous transformation matrix from the tool frame of target robot to the tool frame of sensor robot.
$\boldsymbol{C}$	Homogeneous transformation matrix from the end-flange to the base of target robot.
$\boldsymbol{X}$	Homogeneous transformation matrix from the tool frame to the end-flange of sensor robot.
$\boldsymbol{Y}$	Homogeneous transformation matrix from the base of target robot to the base of sensor robot.
$\boldsymbol{Z}$	Homogeneous transformation matrix from the tool frame to the end-flange of target robot.
$\boldsymbol{T}$	Homogeneous transformation matrix between two different coordinate systems.
$\boldsymbol{R}$	Rotation matrix between two different coordinate systems.
$\boldsymbol{t}$	Translation vector between two different coordinate systems.
$\boldsymbol{g}$	Transformation chain calculated by the dual-robot calibration model.
$\boldsymbol{J}$	Jacobian matrix for the iterative solution.
$e_{\boldsymbol{R}}$	Rotational error of calibration results.
$e_{\boldsymbol{t}}$	Translational error of calibration results.
$SE(3)$	Special Euclidean group in three dimensions.
$SO(3)$	Special Orthogonal group in three dimensions.
$se(3)$	Lie algebra corresponding to $SE(3)$.
$so(3)$	Lie algebra corresponding to $SO(3)$.
$\boldsymbol{\xi}$	Twist associated with the corresponding homogeneous transformation which belongs to Lie algebra $se(3)$.
$\hat{\boldsymbol{\xi}}$	Matrix associated with the corresponding twist which belongs to Lie algebra $se(3)$.
$\boldsymbol{\xi}^{\curlywedge}$	Adjoint of the corresponding element of Lie algebra $se(3)$.
$\delta\boldsymbol{\xi}^{*}$	Optimal perturbation calculated by the iterative method.
$\boldsymbol{\phi}$	Twist associated with the corresponding rotation transformation which belongs to Lie algebra $so(3)$.
$\hat{\boldsymbol{\phi}}$	Skew-symmetric matrix of a twist associated with the corresponding rotational component which belongs to Lie algebra $so(3)$
$\boldsymbol{\rho}$	Translational component of a twist which belongs to Lie algebra $se(3)$.
λ	Lagrange multiplier.
$\mathcal{J}_l(\boldsymbol{\xi})$	Left Jacobian matrix of an element which belongs to Lie algebra $se(3)$.
$\mathcal{J}_r(\boldsymbol{\xi})$	Right Jacobian matrix of an element which belongs to Lie algebra $se(3)$.
$\mathrm{vec}(\bullet)$	Vectorization operator.

Manuscript received 7 June 2023; revised 17 September 2023; accepted 10 December 2023. Date of publication 18 December 2023; date of current version 8 January 2024. This paper was recommended for publication by Associate Editor Sebastien Briot and Editor Eiichi Yoshida upon evaluation of the reviewers' comments. This work was supported in part by the National Natural Science Foundation of China under Grant 52188102, Grant 52090054, and Grant 52075203, and in part by the Basic Research Support Program of HUST under Grant 2023BR009. *(Corresponding author: Wen-long Li.)*

Cheng Jiang, Wen-long Li, Dong-fang Wang, Wei Xu, Huan Zhao, and Han Ding are with the State Key Laboratory of Intelligent Manufacturing Equipment and Technology, Huazhong University of Science and Technology, Wuhan 430074, China (e-mail: msejc@hust.edu.cn; wlli@mail.hust.edu.cn; 978427099@qq.com; weixu.chn@gmail.com; huanzhao@hust.edu.cn; dinghan@mail.hust.edu.cn).

Wen-pan Li is with the Department of Mechanical Engineering, City University of Hong Kong, Hong Kong 999077 (e-mail: wenpanli2-c@my.cityu.edu.hk).

Li-jun Zhu is with the School of Artificial Intelligence and Automation, Huazhong University of Science and Technology, Wuhan 430074, China (e-mail: ljzhu@hust.edu.cn).

Digital Object Identifier 10.1109/TRO.2023.3344025

1941-0468 © 2023 IEEE. Personal use is permitted, but republication/redistribution requires IEEE permission.
See https://www.ieee.org/publications/rights/index.html for more information.

Copyright ©2024 IEEE

Authorized licensed use limited to: Shaanxi Normal University. Downloaded on August 06,2024 at 10:57:59 UTC from IEEE Xplore. Restrictions apply.

$\text{unvec}(\bullet)$	Inverse vectorization operator.
$\otimes$	Kronecker product.
$\|\bullet\|$	Norm of a vector or a matrix.
$[\bullet]^{\vee}$	Map matrix of Lie algebra to the corresponding twist.
$\exp(\bullet)$	Exponential map of a Lie algebra.
$\ln(\bullet)$	Logarithmic map of a Lie algebra.
$\text{Ad}(\bullet)$	Adjoint transformation of a Lie algebra.
$\text{Rot}(\bullet,\bullet)$	Rotation about an axis for a certain angle.
$U(\bullet,\bullet)$	Random number generation function based on uniform distribution.

I. Introduction

MULTIROBOT systems offer several advantages, including efficiency, scalability, and flexibility [1], [2], [3]. Multirobot systems are capable of performing more complex collaborative tasks, particularly for large-scale, intricate structures, compared to single-robot systems. Multirobot equipment has been widely used in various industries, including aviation, aerospace, automotive, and other sectors. Boeing and KUKA have collaborated in developing a multirobot machining system that is a component of fuselage automated upright build for Boeing 777 and 777X aircraft [4]. Airbus also employs comparable automated fuselage structure production lines for the A320 family aircraft [5], with over 20 robots involved in manufacturing the airplane's longer sections. With the support of the European Union's Clean Sky 2 program, Fraunhofer IFAM develops a multirobot assembly system for manufacturing a lighter aircraft fuselage of the future made of thermoplastic fiber-reinforced plastics [6], [7], as shown in Fig. 1. The coordination among multirobots is essential in typical engineering applications, particularly in determining each robot's coordinate relationship.

A multirobot system is essentially a collection of several dual-robot systems. In a dual-robot system, as shown in Fig. 2, the sensor typically serves as a tool mounted on one of the robots to obtain calibration data. The target that can be recognized by the sensor is commonly mounted on the end-flange of the other robot. As such, this article refers to these two robots as the sensor robot and the target robot, respectively. The frames used to describe the robots are $\{S_A\}$, $\{E_A\}$, and $\{L_A\}$, representing the base frame, end-flange frame, and tool frame of the sensor robot. Similarly, the frames for the target robot are $\{S_B\}$, $\{E_B\}$, and $\{L_B\}$, corresponding to the base frame, end-flange frame, and tool frame. Therefore, the dual-robot calibration problem can be formulated as follows:

$$ {}^{S_A}_{E_A}\boldsymbol{T}_i\,{}^{E_A}_{L_A}\boldsymbol{T}\,{}^{L_A}_{L_B}\boldsymbol{T}_i = {}^{S_A}_{S_B}\boldsymbol{T}\,{}^{S_B}_{E_B}\boldsymbol{T}_i\,{}^{E_B}_{L_B}\boldsymbol{T} \tag{1} $$

where ${}^{S_A}_{E_A}\boldsymbol{T}_i$, ${}^{E_A}_{L_A}\boldsymbol{T}$, ${}^{L_A}_{L_B}\boldsymbol{T}_i$, ${}^{S_A}_{S_B}\boldsymbol{T}$, ${}^{S_B}_{E_B}\boldsymbol{T}_i$, and ${}^{E_B}_{L_B}\boldsymbol{T}$ represent the rigid transformation matrices from $\{\boldsymbol{E}_A\}$ to $\{\boldsymbol{S}_A\}$, from $\{\boldsymbol{L}_A\}$ to $\{\boldsymbol{E}_A\}$, from $\{\boldsymbol{L}_B\}$ to $\{\boldsymbol{L}_A\}$, from $\{\boldsymbol{S}_B\}$ to $\{\boldsymbol{S}_A\}$, from $\{\boldsymbol{E}_B\}$ to $\{\boldsymbol{S}_B\}$, and from $\{\boldsymbol{L}_B\}$ to $\{\boldsymbol{E}_B\}$, respectively. To simplify (1), the unknown constant matrices ${}^{E_A}_{L_A}\boldsymbol{T}$, ${}^{S_A}_{S_B}\boldsymbol{T}$, and ${}^{E_B}_{L_B}\boldsymbol{T}$ are represented as $\boldsymbol{X}$, $\boldsymbol{Y}$, and $\boldsymbol{Z}$, respectively. The known matrices ${}^{S_A}_{E_A}\boldsymbol{T}_i$, ${}^{L_A}_{L_B}\boldsymbol{T}_i$, and ${}^{S_B}_{E_B}\boldsymbol{T}_i$ are denoted by $\boldsymbol{A}$, $\boldsymbol{B}$, and $\boldsymbol{C}$, respectively. Equation (1) can be expressed as follows:

Fig. 1. Fraunhofer IFAM develops a multirobot assembly system for manufacturing a lighter aircraft fuselage of the future made of thermoplastic fiber-reinforced plastics (FRP) [6].

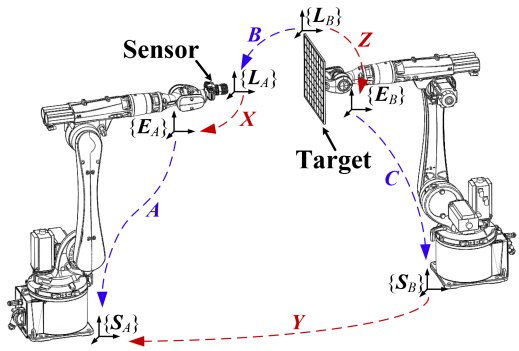

Fig. 2. Problem to calibrate a dual-robot system can be formulated into a matrix equation as $\boldsymbol{AXB} = \boldsymbol{YCZ}$.

$$ \boldsymbol{AXB} = \boldsymbol{YCZ}. \tag{2} $$

The primary objective of dual-robot calibration is to determine the three unknown transformation matrices $\boldsymbol{X}$, $\boldsymbol{Y}$, and $\boldsymbol{Z}$.

A. Related Work

Calibrating a dual-robot system can be regarded as the combination of two single-robot calibration problems. Hand-eye calibration is a well-established problem in single-robot calibration. The research on solving the hand-eye problem can be classified mainly into two forms: $\boldsymbol{AX} = \boldsymbol{XB}$ and $\boldsymbol{AX} = \boldsymbol{YB}$, where $\boldsymbol{X}$ and $\boldsymbol{Y}$ represent unknown transformation matrices. Shiu and Ahmad first introduced the equation $\boldsymbol{AX} = \boldsymbol{XB}$ in [8] to solve the hand-eye calibration problem, where $\boldsymbol{X}$ denotes the unknown transformation from the end-flange to the sensor. The techniques for solving the $\boldsymbol{AX} = \boldsymbol{XB}$ problem can be classified into two categories based on the sequence of solving unknown components, namely separation methods and simultaneous methods. The separation methods separate the unknowns into their rotational and translational components and then solve each of these components one by one. To solve the rotational components, the equations can be converted into a linear system based on distinct representations of the rotation

Authorized licensed use limited to: Shaanxi Normal University. Downloaded on August 06,2024 at 10:57:59 UTC from IEEE Xplore. Restrictions apply.

such as the rotation vector [9], quaternion [10], and Lie algebra [11]. Then, the rotational and translational components can be separated and solved step by step using the least squares method. Errors in the calculation of rotational components can propagate into the solutions of the translational components, creating inaccuracies. To mitigate error transmission, several simultaneous solution methods for the $\boldsymbol{AX} = \boldsymbol{XB}$ problem are proposed. Andreff et al. [12] and Daniilidis [13] convert the $\boldsymbol{AX} = \boldsymbol{XB}$ problem into a homogeneous linear system to solve the rotational and translational components. Meanwhile, Zhao [14] proposed suggested a global optimization method that utilizes quaternion and screw motion constraints to minimize the impact of initial values. Heller et al. [15] proposed a branch and bound optimization method for hand-eye calibration that does not require prior knowledge of a known calibration target. The equation $\boldsymbol{AX} = \boldsymbol{YB}$ is another form of eye-hand calibration problem known as robot-world/hand-eye calibration. The transformation from the robot base to the world coordinate system introduced into the calibration problem. Calibration methods can also be categorized into separation and simultaneous techniques. Separation methods [16], [17] are similar to the $\boldsymbol{AX} = \boldsymbol{XB}$ problems. Li et al. [18] proposed a closed-form solution to solve the problem simultaneously, using dual-quaternions and the Kronecker product. Remy et al. [19] proposed a closed-form solution to solve the problem simultaneously, using dual-quaternions and the Kronecker product. Strobl and Hirzinger [20] introduced a simultaneous iterative method based on a parameterization of a stochastic model. Ernst et al. [21] presented a method for simultaneous tool-flange and robot-world calibration using a least-squares approach, which allows for nonorthogonal matrices. Zhao [22] established a semi-convex objective function based on Kronecker product and dual-quaternion, which can be solved using alternate iteration and linear programming methods. Fu et al. [23], [24] proposed a nonlinear objective model for hand-eye calibration solved by singular value decomposition (SVD).

The dual-robot calibration problem is more complex and harder to linearize and solve than the single-robot system due to the increased and intercoupled unknown matrices. Numerous researchers proposed step-by-step calibration methods for dual-robot systems. Bonitz and Hsia [25] proposed a method to calibrate the base–base transformation of a dual-robot system with physical constraints. Qiao et al. [26] proposed a calibration method for a multirobot system based on the product of exponentials formula to determine the transformation from the robot base to a predetermined coordinate. Zhao et al. [27] proposed a base-frame calibration method based on laser tracker for a dual-machine-based machining system. Zhu et al. [28], [29] introduced a kinematic parameters and tool-flange transformation matrix calibration method for a dual-manipulator system which uses the virtual constraints of the camera optical axis. Ruan et al. [30] suggested a base-frame calibration method for a multirobot cooperative system, utilizing an external three-dimensional (3-D) scanner. Wang et al. [31] presented a plane projection-based method with the point-contact mode for base frame calibration of cooperative manipulators. Yan et al. [32] proposed a closed-form degradation-Kronecker method and an approximate nonlinear method to calibrate a hybrid-robot system. Fu et al. [33] suggested a step-by-step approach based on the dual-quaternion method to determine unknown matrices. Though these methods can be used to calibrate dual-robot systems step by step, they can only obtain one or two unknown transformation matrices, and some specific conditions need to be met to solve the calibration problem. Unfortunately, the accumulation of errors in each step of the calculation may lead to an unreliable calibration result.

In order to minimize calibration errors associated with step-by-step approaches, it is crucial to develop simultaneous calibration methods. Wu et al. [34], [35], Ma et al. [36], Wang et al. [37], Jiang et al. [38], and Qin et al. [39] proposed different techniques for simultaneously solving $\boldsymbol{AXB} = \boldsymbol{YCZ}$ problem. Wu et al. [34], [35] proposed an iterative approach for calibrating dual-robots by using the Lie algebra representation of $SO(3)$ to solve rotational components and utilized the first-order approximation of the exponential mapping of Lie algebra to determine the optimization result. Ma et al. [36] proposed various techniques, including two probabilistic methods and a hybrid technique, for solving the dual-robot calibration problem without prior knowledge of data correspondence. Wang et al. [37] introduced both a closed-form method based on the Kronecker product and an iterative technique to optimize rotational and translational components of unknown values. By including orthogonal constraints on the rotation matrix, the objective function is improved, and optimization results were achieved using the stochastic variance reduced gradient (SVRG) algorithm. Similarly, Qin [39] presented an iterative method based on the Levenberg–Marquardt (L-M) algorithm to calibrate rotational components of dual-robot systems simultaneously. They obtained the initial value through a hand-eye calibration process. Although Wu's and Qin's methods can simultaneously calibrate rotational components, they determine translational components separately. However, Ma's probabilistic method is susceptible to noise, and the hybrid approach increases computational costs due to introducing Yan's or Wu's techniques. Additionally, Wang's iterative approach introduces penalty factors that may result in unstable solutions.

A typical dual-robot calibration model includes three known matrices $\boldsymbol{A}$, $\boldsymbol{B}$, and $\boldsymbol{C}$ and three unknown matrices $\boldsymbol{X}$, $\boldsymbol{Y}$, and $\boldsymbol{Z}$ that are coupled with one another. The linear methods are difficult for solving the unknown matrices simultaneously, and the existing nonlinear methods can only solve unknown rotational components. Therefore, the unknown translational components require a separate solution that results in error transmission, subsequently reducing the calibration accuracy of dual-robot systems. Given that the path of the robots depends on the relative relationship between them, poor calibration results can lead to poor position accuracy and negatively impact the accuracy of robotic operation.

B. Contribution

This article proposes a dual-robot accurate calibration method based on convex optimization and Lie derivative. A unified convex optimization model with a quadratic form is established

Authorized licensed use limited to: Shaanxi Normal University. Downloaded on August 06,2024 at 10:57:59 UTC from IEEE Xplore. Restrictions apply.

to simultaneously solve all the unknown rotational and translational components using Lie group representation of $SE(3)$. The Jacobian matrix of the proposed model is derived explicitly using the Lie derivative of $SE(3)$ because of the smoothness of the Lie group $SE(3)$. In order to balance the impact of the magnitudes of rotational and translational optimization variables on the optimization results, a weight coefficient for the optimization variables is defined based on the norm of the initial calibration results. Moreover, this article proposes a dual-robot initial calibration method based on a two-step vectorization technique to estimate optimal weight coefficients and improve iteration efficiency. Combining initial calibration, the proposed convex optimization model can obtain an accurate calibration result. The proposed method has two main advantages.

1) *High Accuracy:* Due to closedness of Lie group, the proposed calibration method using Lie derivative ensures high accuracy and orthogonality of the rotational components. Results do not require additional orthogonalization, and the proposed calibration simultaneously solves rotational and translational components of all unknown matrices, thus avoiding error transmission and accumulation.
2) *High Stability:* Due to smoothness of Lie group, the proposed quadratic form optimization model ensures higher stability and convergence of the solution. The Jacobian matrix of the model is explicitly derived by the corresponding Lie derivative of $SE(3)$, which allows for the utilization of common Newton-like iterative methods to simultaneously determine an optimal solution.

The structure of this article is organized as follows: Section II proposes the convex optimization model for accurate calibration and defines the weighting coefficients for optimization variables. Section III presents a closed-form method for initial calibration and summaries the entire calibration procedure. In Section IV, the experiments are carried out to evaluate the effectiveness and performance of the proposed method. Finally, Section V concludes this article.

II. Accurate Calibration Using Convex Optimization

In order to accurately solve the unknown parameters of a dual robot system, a convex optimization model for dual-robot calibration based on Lie group $SE(3)$ is established in this section, using the spatial transformation chain of the dual robot system. The solution method of the model is derived using Lie derivatives.

A. Convex Optimization Model for Dual-Robot Calibration

This section proposes a nonlinear iterative method employing the Lie algebra and Lie derivative principles of $SE(3)$ to obtain accurate calibration results. The transformation chain $\boldsymbol{g}$ of a dual-robot system can be obtained through (2)

$$\boldsymbol{g} = \boldsymbol{AXBZ}^{-1}\boldsymbol{C}^{-1}\boldsymbol{Y}^{-1} = \boldsymbol{I}_4. \tag{3}$$

Ideally, the transformation chain $\boldsymbol{g}_n$ is an identity matrix. However, in the actual calibration process, the actual transformation chain $\boldsymbol{g}_a$ is generally not equal to the identity matrix due to the presence of measurement noise and system errors. Therefore, the calibration error $\boldsymbol{e}$ can be defined as follows:

$$\boldsymbol{e} = \boldsymbol{g}_a\boldsymbol{g}_n^{-1}. \tag{4}$$

To simplify the representation of the calibration error and facilitate the computation of the gradient matrix, the proposed optimization method incorporates the Lie algebra representation of $SE(3)$. According to Lie theory, rigid transformations belong to the special Euclidean group $SE(3)$, and their corresponding Lie algebra $se(3)$ can be represented as a twist

$$\boldsymbol{\xi} = \begin{bmatrix}\boldsymbol{\rho}^{\mathrm{T}} & \boldsymbol{\phi}^{\mathrm{T}}\end{bmatrix}^{\mathrm{T}} \tag{5}$$

where $\boldsymbol{\rho} \in \mathbb{R}^3$ is a vector associated with its translational component, whereas $\boldsymbol{\phi} \in \mathbb{R}^3$ is a twist associated with its rotational component. The exponential map defines the mapping from Lie algebra $se(3)$ to Lie group $SE(3)$

$$\boldsymbol{T} = \exp\left(\hat{\boldsymbol{\xi}}\right) \in SE\,(3) \tag{6}$$

where $\hat{\boldsymbol{\xi}} \in \mathbb{R}^{4\times4}$ represents matrix form of Lie algebra $se(3)$, and the operator "$\wedge$" for $se(3)$ maps $\boldsymbol{\xi}$ into $\hat{\boldsymbol{\xi}}$. A detailed description of the relationship between Lie algebra $se(3)$ and Lie group $SE(3)$ can be found in Appendix A. Let $\boldsymbol{A} = \exp(\hat{\boldsymbol{\xi}}_A)$, $\boldsymbol{B} = \exp(\hat{\boldsymbol{\xi}}_B)$, $\boldsymbol{C} = \exp(\hat{\boldsymbol{\xi}}_C)$, $\boldsymbol{X} = \exp(\hat{\boldsymbol{\xi}}_X)$, $\boldsymbol{Y} = \exp(\hat{\boldsymbol{\xi}}_Y)$, and $\boldsymbol{Z} = \exp(\hat{\boldsymbol{\xi}}_Z)$, the transformation chain (3) can be expressed by Lie algebra $se(3)$ as follows:

$$\begin{aligned}\boldsymbol{g}_a = {} & \exp\left(\boldsymbol{\xi}_{A_i}\right)\exp\left(\boldsymbol{\xi}_X\right)\exp\left(\boldsymbol{\xi}_{B_i}\right) \\ & \times \exp\left(-\boldsymbol{\xi}_Z\right)\exp\left(-\boldsymbol{\xi}_{C_i}\right)\exp\left(-\boldsymbol{\xi}_Y\right)\end{aligned} \tag{7}$$

where the symbol "$\times$" represents the multiplication of matrices. To optimize the calibration error $\boldsymbol{e}$, the proposed model uses linearization technique to construct an optimization objective function. According to the definition of the logarithmic mapping, the calibration error $\boldsymbol{e}$ can be expanded and represented as follows:

$$\ln\left(\boldsymbol{e}\right) = \ln\left(\boldsymbol{g}_a\boldsymbol{g}_n^{-1}\right) = \sum_{k=1}^{\infty}(-1)^{k-1}\frac{\left(\boldsymbol{g}_a\boldsymbol{g}_n^{-1} - \boldsymbol{I}_4\right)^k}{k}. \tag{8}$$

Using the first-order approximation, (8) can be expressed as follows:

$$\begin{aligned}\ln\left(\boldsymbol{e}\right) &\approx \boldsymbol{g}_a\boldsymbol{g}_n^{-1} - \boldsymbol{I}_4 \\ &= \left(\boldsymbol{g}_a - \boldsymbol{g}_n\right)\boldsymbol{g}_n^{-1} \\ &= \delta\boldsymbol{g}\boldsymbol{g}^{-1}.\end{aligned} \tag{9}$$

The calibration error $\boldsymbol{e}$ can be expressed as $\delta\boldsymbol{g}\boldsymbol{g}^{-1}$. Furthermore, the differential term $\delta\boldsymbol{g}$ can be represented as the sum of the differential term of each optimization objective and the product of its partial differential

$$\delta\boldsymbol{g}\boldsymbol{g}^{-1} = \left(\frac{\partial\boldsymbol{g}}{\partial\boldsymbol{\xi}_X}\delta\boldsymbol{\xi}_X + \frac{\partial\boldsymbol{g}}{\partial\boldsymbol{\xi}_Y}\delta\boldsymbol{\xi}_Y + \frac{\partial\boldsymbol{g}}{\partial\boldsymbol{\xi}_Z}\delta\boldsymbol{\xi}_Z\right)\boldsymbol{g}^{-1}. \tag{10}$$

Therefore, the calibration of a dual-robot can be considered as the minimization optimization problem of unknown twists $\boldsymbol{\xi}_X, \boldsymbol{\xi}_Y, \boldsymbol{\xi}_Z$. Based on the calibration dataset, a minimization objective function is constructed by summing the deviations

Authorized licensed use limited to: Shaanxi Normal University. Downloaded on August 06,2024 at 10:57:59 UTC from IEEE Xplore. Restrictions apply.

between the calibration error $\boldsymbol{e}$ and the differential term $\delta \boldsymbol{g}\boldsymbol{g}^{-1}$ calculated for each set of calibration data

$$\underset{\delta\boldsymbol{\xi}_X,\delta\boldsymbol{\xi}_Y,\delta\boldsymbol{\xi}_Z}{\arg\min} \times \sum \left\| \ln\left(\boldsymbol{e}\right) - \left(\frac{\partial \boldsymbol{g}}{\partial \boldsymbol{\xi}_X}\delta\boldsymbol{\xi}_X + \frac{\partial \boldsymbol{g}}{\partial \boldsymbol{\xi}_Y}\delta\boldsymbol{\xi}_Y + \frac{\partial \boldsymbol{g}}{\partial \boldsymbol{\xi}_Z}\delta\boldsymbol{\xi}_Z \right) \boldsymbol{g}^{-1} \right\|^2. \tag{11}$$

The objective function is a convex optimization problem with a quadratic form. Adding translational constraints creates a more fully constrained optimization solution compared to rotational constraints alone. It should be noted that although the proposed model is a convex optimization model, it uses linearization to construct the optimization objective function. Therefore, its convergence still requires an effective guarantee in a reasonable initial value neighborhood.

B. Iterative Solution Using Lie Derivative

To quickly obtained the optimal solution, the Jacobian matrix of the objective function is explicitly derived using the Lie derivative of $SE(3)$. Define the operator "$\vee$" as a mapping from $\hat{\boldsymbol{\xi}} \in se(3)$ to $\boldsymbol{\xi} \in \mathbb{R}^6$, the deviation term $\delta \boldsymbol{g}\boldsymbol{g}^{-1}$ can be expressed by $\delta\boldsymbol{\xi}_X$, $\delta\boldsymbol{\xi}_Y$, and $\delta\boldsymbol{\xi}_Z$ as follows:

$$\begin{aligned}
&\left[\delta \boldsymbol{g}\boldsymbol{g}^{-1}\right]^{\vee} \\
&= \left[\exp\left(\boldsymbol{\xi}_{A_i}\right)\delta\exp\left(\boldsymbol{\xi}_X\right)\exp\left(-\boldsymbol{\xi}_X\right)\exp\left(-\boldsymbol{\xi}_{A_i}\right)\right]^{\vee} \\
&\quad + \begin{bmatrix}\exp\left(\boldsymbol{\xi}_{A_i}\right)\exp\left(\boldsymbol{\xi}_X\right)\exp\left(\boldsymbol{\xi}_{B_i}\right)\delta\exp\left(-\boldsymbol{\xi}_Z\right) \\ \times\exp\left(\boldsymbol{\xi}_Z\right)\exp\left(-\boldsymbol{\xi}_{B_i}\right)\exp\left(-\boldsymbol{\xi}_X\right)\exp\left(-\boldsymbol{\xi}_{A_i}\right)\end{bmatrix}^{\vee} \\
&\quad + \begin{bmatrix}\exp\left(\boldsymbol{\xi}_{A_i}\right)\exp\left(\boldsymbol{\xi}_X\right)\exp\left(\boldsymbol{\xi}_{B_i}\right)\exp\left(-\boldsymbol{\xi}_Z\right) \\ \times\exp\left(-\boldsymbol{\xi}_{C_i}\right)\delta\exp\left(-\boldsymbol{\xi}_Y\right)\exp\left(\boldsymbol{\xi}_Y\right)\exp\left(\boldsymbol{\xi}_{C_i}\right) \\ \times\exp\left(\boldsymbol{\xi}_Z\right)\exp\left(-\boldsymbol{\xi}_{B_i}\right)\exp\left(-\boldsymbol{\xi}_X\right)\exp\left(-\boldsymbol{\xi}_{A_i}\right)\end{bmatrix}^{\vee} \\
&= Ad\left(\exp\left(\boldsymbol{\xi}_{A_i}\right)\right)\left[\delta\exp\left(\boldsymbol{\xi}_X\right)\exp\left(-\boldsymbol{\xi}_X\right)\right]^{\vee} \\
&\quad + Ad\left(\exp\left(\boldsymbol{\xi}_{A_i}\right)\exp\left(\boldsymbol{\xi}_X\right)\exp\left(\boldsymbol{\xi}_{B_i}\right)\right) \\
&\quad \times\left[\delta\exp\left(-\boldsymbol{\xi}_Z\right)\exp\left(\boldsymbol{\xi}_Z\right)\right]^{\vee} \\
&\quad + Ad\left(\exp\left(\boldsymbol{\xi}_{A_i}\right)\exp\left(\boldsymbol{\xi}_X\right)\exp\left(\boldsymbol{\xi}_{B_i}\right)\exp\left(-\boldsymbol{\xi}_Z\right)\exp\left(-\boldsymbol{\xi}_{C_i}\right)\right) \\
&\quad \times\left[\delta\exp\left(-\boldsymbol{\xi}_Y\right)\exp\left(\boldsymbol{\xi}_Y\right)\right]^{\vee}
\end{aligned} \tag{12}$$

where the operator $Ad(\boldsymbol{.})$ represents the adjoint of an element belonging to $SE(3)$, as detailed in Appendix B. Using the approximate Baker–Campbell–Hausdorff formulas, the deviation $\delta\exp(-\boldsymbol{\xi})\exp(\boldsymbol{\xi})$ term can be further approximated as

$$\begin{aligned}
&\left[\delta\exp\left(\boldsymbol{\xi}\right)\exp\left(-\boldsymbol{\xi}\right)\right]^{\vee} \\
&= \left[\exp\left(\boldsymbol{\xi}+\delta\boldsymbol{\xi}\right) - \exp\left(\boldsymbol{\xi}\right)\right]\exp\left(-\boldsymbol{\xi}\right) \\
&= \exp\left(\boldsymbol{\xi}+\delta\boldsymbol{\xi}\right)\exp\left(-\boldsymbol{\xi}\right) - \boldsymbol{I}_4 \\
&\approx \ln\left[\left(\boldsymbol{\xi}+\delta\boldsymbol{\xi}\right)\exp\left(-\boldsymbol{\xi}\right)\right] \\
&= \mathcal{J}_l\left(\boldsymbol{\xi}\right)\delta\boldsymbol{\xi}
\end{aligned} \tag{13}$$

Where $\mathcal{J}_l(\boldsymbol{\xi})$ represents the left Jacobian matrix of an element belonging to $se(3)$. The left Jacobian matrix of an element belonging to $se(3)$ is defined as follows:

$$\begin{aligned}
\mathcal{J}_l\left(\boldsymbol{\xi}\right) = \boldsymbol{I}_6 &+ \left(\frac{4-\phi\sin\phi-4\cos\phi}{2\phi^2}\right)\boldsymbol{\xi}^{\curlywedge} \\
&+ \left(\frac{4\phi-5\sin\phi-\phi\cos\phi}{2\phi^3}\right)\left(\boldsymbol{\xi}^{\curlywedge}\right)^2 \\
&+ \left(\frac{2-\phi\sin\phi-2\cos\phi}{2\phi^4}\right)\left(\boldsymbol{\xi}^{\curlywedge}\right)^3 \\
&+ \left(\frac{2\phi-3\sin\phi-\phi\cos\phi}{2\phi^5}\right)\left(\boldsymbol{\xi}^{\curlywedge}\right)^4
\end{aligned} \tag{14}$$

where $\boldsymbol{\xi}^{\curlywedge}$ is the adjoint of an element of $se(3)$, as referenced in Appendix B. The deviation $\delta \boldsymbol{g}\boldsymbol{g}^{-1}$ in (12) can be expressed as follows:

$$\left[\delta \boldsymbol{g}\boldsymbol{g}^{-1}\right]^{\vee} = \boldsymbol{J}_X\delta\boldsymbol{\xi}_X + \boldsymbol{J}_Y\delta\boldsymbol{\xi}_Y + \boldsymbol{J}_Z\delta\boldsymbol{\xi}_Z \tag{15}$$

where $\boldsymbol{J}_X$, $\boldsymbol{J}_Y$, and $\boldsymbol{J}_Z$ are defined as follows:

$$\boldsymbol{J}_X = Ad\left(\exp\left(\boldsymbol{\xi}_{A_i}\right)\right)\mathcal{J}_l\left(\boldsymbol{\xi}_X\right) \tag{16}$$

$$\boldsymbol{J}_Y = Ad\left(\begin{array}{l}\exp\left(\boldsymbol{\xi}_{A_i}\right)\exp\left(\boldsymbol{\xi}_X\right)\exp\left(\boldsymbol{\xi}_{B_i}\right) \\ \exp\left(-\boldsymbol{\xi}_Z\right)\exp\left(-\boldsymbol{\xi}_{C_i}\right)\end{array}\right)\mathcal{J}_r\left(\boldsymbol{\xi}_Y\right) \tag{17}$$

$$\boldsymbol{J}_Z = Ad\left(\exp\left(\boldsymbol{\xi}_{A_i}\right)\exp\left(\boldsymbol{\xi}_X\right)\exp\left(\boldsymbol{\xi}_{B_i}\right)\right)\mathcal{J}_r\left(\boldsymbol{\xi}_Z\right) \tag{18}$$

where $\mathcal{J}_r(\boldsymbol{\xi})$ represents the right Jacobian matrix of an element belonging to $se(3)$. The right Jacobian matrix of an element belonging to $se(3)$ can be calculated by the corresponding left Jacobian matrix

$$\mathcal{J}_r\left(\boldsymbol{\xi}\right) = \mathcal{J}_l\left(-\boldsymbol{\xi}\right). \tag{19}$$

Let $\boldsymbol{J}_{XYZ} = [\boldsymbol{J}_X \ \ \boldsymbol{J}_Y \ \ \boldsymbol{J}_Z]$, $\delta\boldsymbol{\xi}_{XYZ} = [\delta\boldsymbol{\xi}_X^{\mathrm{T}} \ \delta\boldsymbol{\xi}_Y^{\mathrm{T}} \ \ \delta\boldsymbol{\xi}_Z^{\mathrm{T}}]^{\mathrm{T}}$. The formula (15) can be further simplified as follows:

$$\left[\delta \boldsymbol{g}\boldsymbol{g}^{-1}\right]^{\vee} = \boldsymbol{J}_{XYZ}\delta\boldsymbol{\xi}_{XYZ}. \tag{20}$$

The objective function (11) can be rewritten as follows:

$$\underset{\delta\boldsymbol{\xi}_{XYZ}}{\arg\min}\ \frac{1}{2}\sum_{i=1}^{n}\left\|\ln\left(\boldsymbol{e}\right) - \boldsymbol{J}_{XYZ}\delta\boldsymbol{\xi}_{XYZ}\right\|^2 \tag{21}$$

where n represents the number of samples used for calibration. Then, the Newton-like methods, such as G-N or L-M method, can be used to calculate optimal perturbation $\delta\boldsymbol{\xi}^*_{XYZ_{op}}$, consisting of $\delta\hat{\boldsymbol{\xi}}^*_{X_{op}}$, $\delta\hat{\boldsymbol{\xi}}^*_{Y_{op}}$, and $\delta\hat{\boldsymbol{\xi}}^*_{Z_{op}}$. The optimal perturbation, denoted as $\delta\boldsymbol{\xi}^*_{XYZ_{op}}$, is then used to update optimization objectives until the stopping criteria are satisfied

$$\exp\left(\hat{\boldsymbol{\xi}}_{X_{op}}\right) = \exp\left(\hat{\boldsymbol{\xi}}_{X_0} + \delta\hat{\boldsymbol{\xi}}^*_{X_{op}}\right) \tag{22}$$

$$\exp\left(\hat{\boldsymbol{\xi}}_{Y_{op}}\right) = \exp\left(\hat{\boldsymbol{\xi}}_{Y_0} + \delta\hat{\boldsymbol{\xi}}^*_{Y_{op}}\right) \tag{23}$$

$$\exp\left(\hat{\boldsymbol{\xi}}_{Z_{op}}\right) = \exp\left(\hat{\boldsymbol{\xi}}_{Z_0} + \delta\hat{\boldsymbol{\xi}}^*_{Z_{op}}\right) \tag{24}$$

where $\hat{\boldsymbol{\xi}}_{X_0}$, $\hat{\boldsymbol{\xi}}_{Y_0}$, and $\hat{\boldsymbol{\xi}}_{Z_0}$ are initial value for iteration. Due to the introduction of Lie algebra and corresponding Lie derivative, the proposed method ensures that the rotational components remain orthogonal through the closure of Lie algebra. Simultaneously solving the unknown rotational and translational components

Authorized licensed use limited to: Shaanxi Normal University. Downloaded on August 06,2024 at 10:57:59 UTC from IEEE Xplore. Restrictions apply.

in the proposed method prevents the accumulation and transmission of errors. The proposed iterative model for accurate calibration is in quadratic form, which ensures its convergence. The proposed model's Jacobian matrix is explicitly derived through Lie derivatives and can be solved with Newton-like iterative methods.

C. Weighting Coefficient for Optimization of Rotational and Translational Components

In Section II-A, the Jacobian matrices $\boldsymbol{J}_{XYZ}$ and the transformation chain error $\boldsymbol{e}$ are directly calculated by known and optimization twists. However, since rotational and translational components have varying physical units, their optimization variables may differ greatly in orders of magnitude. This can cause variables with larger magnitudes to overshadow the contributions of smaller magnitude variables to the objective function, resulting in deviations of the smaller magnitude variables from their expected values. To address this problem, weight coefficients are utilized to balance the influence of rotational and translational variables' magnitudes on the optimization process. The magnitude of rotational and translational variables can be represented by the norm of the corresponding part in a twist. Therefore, weight coefficients can be determined based on better initial calibration results $\boldsymbol{\xi}_{X_0}$, $\boldsymbol{\xi}_{Y_0}$, and $\boldsymbol{\xi}_{Z_0}$. Weight coefficient w_ρ, for translational variables, is defined as follows:

$$w_\rho = \frac{1}{3}\left(\left\|\boldsymbol{\rho}_{X_0}\right\| + \left\|\boldsymbol{\rho}_{Y_0}\right\| + \left\|\boldsymbol{\rho}_{Z_0}\right\|\right). \tag{25}$$

For rotational components, weight coefficient w_ϕ is defined as follows:

$$w_\phi = \frac{1}{3}\left(\left\|\boldsymbol{\phi}_{X_0}\right\| + \left\|\boldsymbol{\phi}_{Y_0}\right\| + \left\|\boldsymbol{\phi}_{Z_0}\right\|\right). \tag{26}$$

According to (71) in Appendix A, a translational vector $\boldsymbol{\rho}$ of a twist and the corresponding translational component $\boldsymbol{t}$ in Euclidean space are linear relationship. Therefore, weight coefficients can be applied to scale the magnitude of the translational vector in the twist, while the scaling of the rotational twist $\boldsymbol{\phi}$ does not change. After scaling, the twist for optimization is defined as follows:

$$\boldsymbol{\xi}' = \begin{bmatrix}\boldsymbol{\rho}' \\ \boldsymbol{\phi}\end{bmatrix} = \begin{bmatrix}\frac{w_\phi}{w_\rho}\boldsymbol{\rho} \\ \boldsymbol{\phi}\end{bmatrix}. \tag{27}$$

This scaling enables optimization variables to have similar orders of magnitude, allowing for a more balanced contribution of rotational and translational variables to optimization process. In Section II-A, the scaling twists $\boldsymbol{\xi}'_A$, $\boldsymbol{\xi}'_B$, $\boldsymbol{\xi}'_C$, $\boldsymbol{\xi}'_{X_0}$, $\boldsymbol{\xi}'_{Y_0}$, and $\boldsymbol{\xi}'_{Z_0}$ replace the corresponding twists. Following optimization, the translational vector $\boldsymbol{\rho}$ of the final results must be divided by the weight coefficient's reciprocal value. This is necessary to ensure that the final results have the correct magnitude after scaling

$$\boldsymbol{\xi} = \begin{bmatrix}\frac{w_\rho}{w_\phi}\boldsymbol{\rho}' \\ \boldsymbol{\phi}\end{bmatrix}. \tag{28}$$

III. Initial Calibration Using Two-Step Linearization

The optimization model proposed in Section II-A is a convex optimization model with a quadratic form. In theory, this model does not have special requirements for the selection of initial values. However, since linearization is used in the optimization process, its good convergence requires an effective guarantee in a reasonable initial value neighborhood. In addition, the optimization variable weight coefficient proposed in Section II-C also has an impact on the optimization results, and the estimation of this weight coefficient also requires a reasonable initial value. Furthermore, better initial values can also improve the convergence speed of iteration. In this section, an evolved two-step linear closed-form method for initial calibration, motivated by the closed-form method presented by Wang et al. [37], is proposed for the estimation of initial calibration results.

A. Solution for Rotational Components $\boldsymbol{R}_Y$

During actual dual-robot calibration, n sets of measured data $\boldsymbol{A}_i$, $\boldsymbol{B}_i$, and $\boldsymbol{C}_i$ $(i = 1, 2, \ldots, n)$ are obtained by changing the postures of two robots. The equations of rotational and translational components can be derived by expanding $\boldsymbol{A}_i\boldsymbol{X}\boldsymbol{B}_i = \boldsymbol{Y}\boldsymbol{C}_i\boldsymbol{Z}$

$$\boldsymbol{R}_{A_i}\boldsymbol{R}_X\boldsymbol{R}_{B_i} = \boldsymbol{R}_Y\boldsymbol{R}_{C_i}\boldsymbol{R}_Z \tag{29}$$

$$\boldsymbol{R}_{A_i}\boldsymbol{R}_X\boldsymbol{t}_{B_i} + \boldsymbol{R}_{A_i}\boldsymbol{t}_X + \boldsymbol{t}_{A_i} = \boldsymbol{R}_Y\boldsymbol{R}_{C_i}\boldsymbol{t}_Z + \boldsymbol{R}_Y\boldsymbol{t}_{C_i} + \boldsymbol{t}_Y \tag{30}$$

where $\boldsymbol{R}$ is the corresponding rotation matrix with dimensions of 3×3, and $\boldsymbol{t}$ is the corresponding translation vector with dimensions of 3×1. Equations (29) and (30) have intercoupling between the unknown rotational and translational components, specifically $\boldsymbol{R}_X$, $\boldsymbol{R}_Y$ $\boldsymbol{R}_Z$, $\boldsymbol{t}_X$, $\boldsymbol{t}_Y$, and $\boldsymbol{t}_Z$. Direct linearization of all unknown matrices is a challenging task as a one-step linearization operation cannot decouple the unknown components. Thus, to decouple the unknown components, a two-step vectorization method is proposed. By using two sets of arbitrary measured data, the rotational equations can be derived as follows:

$$\begin{cases}\boldsymbol{R}_{A_j}\boldsymbol{R}_X\boldsymbol{R}_{B_j} = \boldsymbol{R}_Y\boldsymbol{R}_{C_j}\boldsymbol{R}_Z \\ \boldsymbol{R}_{A_k}\boldsymbol{R}_X\boldsymbol{R}_{B_k} = \boldsymbol{R}_Y\boldsymbol{R}_{C_k}\boldsymbol{R}_Z\end{cases} \tag{31}$$

where subscripts j and k represent order of measurement data. Because $\boldsymbol{R}_Y$ can be considered as a constant homogeneous transformation matrix, the following equation can be obtained from (31) by eliminating $\boldsymbol{R}_Y$:

$$\boldsymbol{R}_{A_j}\boldsymbol{R}_X\boldsymbol{R}_{B_j}\boldsymbol{R}_Z^{-1}\boldsymbol{R}_{C_j}^{-1} = \boldsymbol{R}_{A_k}\boldsymbol{R}_X\boldsymbol{R}_{B_k}\boldsymbol{R}_Z^{-1}\boldsymbol{R}_{C_k}^{-1}. \tag{32}$$

Both sides of (32) are left multiplied by $\boldsymbol{R}_{A_k}^{-1}$ and right multiplied $\boldsymbol{R}_{C_k}$ simultaneously

$$\left(\boldsymbol{R}_{A_k}^{-1}\boldsymbol{R}_{A_j}\right)\boldsymbol{R}_X\boldsymbol{R}_{B_j}\boldsymbol{R}_Z^{-1} = \boldsymbol{R}_X\boldsymbol{R}_{B_k}\boldsymbol{R}_Z^{-1}\left(\boldsymbol{R}_{C_k}^{-1}\boldsymbol{R}_{C_j}\right). \tag{33}$$

$\boldsymbol{R}_{A_k}^{-1}\boldsymbol{R}_{A_j}$ and $\boldsymbol{R}_{C_j}^{-1}\boldsymbol{R}_{C_k}$ are relative changes of two robot end-flange frame. Let $\boldsymbol{R}_{A_{jk}} = \boldsymbol{R}_{A_k}^{-1}\boldsymbol{R}_{A_j}$ and $\boldsymbol{R}_{C_{jk}} = \boldsymbol{R}_{C_k}^{-1}\boldsymbol{R}_{C_j}$, (33) can be rewritten as follows:

$$\boldsymbol{R}_{A_{jk}}\boldsymbol{R}_X\boldsymbol{R}_{B_j}\boldsymbol{R}_Z^{-1} = \boldsymbol{R}_X\boldsymbol{R}_{B_k}\boldsymbol{R}_Z^{-1}\boldsymbol{R}_{C_{jk}}. \tag{34}$$

Authorized licensed use limited to: Shaanxi Normal University. Downloaded on August 06,2024 at 10:57:59 UTC from IEEE Xplore. Restrictions apply.

Using column vectorization operator vec($\bullet$), the first-step vectorization is applied to both sides of (34)

$$\text{vec}\left(\boldsymbol{R}_{A_{jk}}\left(\boldsymbol{R}_X\boldsymbol{R}_{B_j}\boldsymbol{R}_Z^{-1}\right)\right)=\text{vec}\left(\left(\boldsymbol{R}_X\boldsymbol{R}_{B_k}\boldsymbol{R}_Z^{-1}\right)\boldsymbol{R}_{C_{jk}}\right). \tag{35}$$

By introducing the Kronecker product, (35) can be further written as follows:

$$\begin{aligned}&\left(\boldsymbol{I}_3\otimes\boldsymbol{R}_{A_{jk}}\right)\left(\boldsymbol{R}_Z\otimes\boldsymbol{R}_X\right)\text{vec}\left(\boldsymbol{R}_{B_j}\right)\\&=\left(\boldsymbol{R}_{C_{jk}}^{\mathrm{T}}\otimes\boldsymbol{I}_3\right)\left(\boldsymbol{R}_Z\otimes\boldsymbol{R}_X\right)\text{vec}\left(\boldsymbol{R}_{B_k}\right)\end{aligned} \tag{36}$$

where the symbol $\otimes$ represents the Kronecker product, the subscript of the identity matrix indicates the size of the matrix. Note that there is a strong coupling between $\boldsymbol{R}_X$ and $\boldsymbol{R}_Z$ in (36). Since both $\boldsymbol{R}_X$ and $\boldsymbol{R}_Z$ are constant, $\boldsymbol{R}_Z\otimes\boldsymbol{R}_X$ can also be regards as an unknown constant matrix. Let $\boldsymbol{L}_{jk}=\boldsymbol{I}_3\otimes\boldsymbol{R}_{A_{jk}}$, $\boldsymbol{M}_{ZX}=\boldsymbol{R}_Z\otimes\boldsymbol{R}_X$, $\boldsymbol{N}_{jk}=\boldsymbol{R}_{C_{jk}}^{\mathrm{T}}\otimes\boldsymbol{I}_3$, $\boldsymbol{m}_{B_i}=\text{vec}(\boldsymbol{R}_{B_i})$, (36) can be simplified as follows:

$$\boldsymbol{L}_{jk}\boldsymbol{M}_{ZX}\boldsymbol{m}_{B_j}=\boldsymbol{N}_{jk}\boldsymbol{M}_{ZX}\boldsymbol{m}_{B_j}. \tag{37}$$

To linearize the unknown matrix, the second-step vectorization is applied to both sides of (37)

$$\text{vec}\left(\boldsymbol{L}_{jk}\boldsymbol{M}_{ZX}\boldsymbol{m}_{B_j}\right)=\text{vec}\left(\boldsymbol{N}_{jk}\boldsymbol{M}_{ZX}\boldsymbol{m}_{B_k}\right) \tag{38}$$

$$\left(\boldsymbol{m}_{B_j}^{\mathrm{T}}\otimes\boldsymbol{L}_{jk}\right)\text{vec}\left(\boldsymbol{M}_{ZX}\right)=\left(\boldsymbol{m}_{B_k}^{\mathrm{T}}\otimes\boldsymbol{N}_{jk}\right)\text{vec}\left(\boldsymbol{M}_{ZX}\right). \tag{39}$$

Using the two-step vectorization processing, (39) is rewritten as a homogeneous linear system

$$\left(\left(\boldsymbol{m}_{B_j}^{\mathrm{T}}\otimes\boldsymbol{L}_{jk}\right)-\left(\boldsymbol{m}_{B_k}^{\mathrm{T}}\otimes\boldsymbol{N}_{jk}\right)\right)\text{vec}\left(\boldsymbol{M}_{ZX}\right)=\boldsymbol{0}. \tag{40}$$

Let $\boldsymbol{U}_i=(\boldsymbol{m}_{B_j}^{\mathrm{T}}\otimes\boldsymbol{L}_{jk})-(\boldsymbol{m}_{B_k}^{\mathrm{T}}\otimes\boldsymbol{N}_{jk})$ and $\boldsymbol{m}_{ZX}=\text{vec}(\boldsymbol{M}_{ZX})$, (40) can be simplified as follows:

$$\boldsymbol{U}_i\boldsymbol{m}_{ZX}=\boldsymbol{0}. \tag{41}$$

Assuming there are n sets of measured data $\boldsymbol{A}_i$, $\boldsymbol{B}_i$, and $\boldsymbol{C}_i$ $(i=1,2,\ldots,n)$, there are $n-1$ pairs of relative rotation matrices $\boldsymbol{R}_{A_{jk}}$ and $\boldsymbol{R}_{C_{jk}}$ $(j=1,2,\ldots,n-1,\ k=2,\ldots,n,k=j+1)$ calculated by these data. Let $\tilde{\boldsymbol{U}}=[\boldsymbol{U}_1;\boldsymbol{U}_2;\ldots;\boldsymbol{U}_{n-1}]$, the complete equation about $\boldsymbol{m}_{ZX}$ can be obtained

$$\tilde{\boldsymbol{U}}\boldsymbol{m}_{ZX}=\boldsymbol{0}. \tag{42}$$

For obtaining a non-trivial solution ($\boldsymbol{m}_{ZX}\neq\boldsymbol{0}$), (42) must be an overdetermined homogeneous linear system. Thus, there are more independent equations than unknowns ($n>10$). Due to noise and error, it is unlikely to find an exact nontrivial solution to the overdetermined system. The solution can be calculated by minimizing the algebraic distance $\|\tilde{\boldsymbol{U}}\boldsymbol{m}_{ZX}\|$ between them

$$\arg\min_{\boldsymbol{m}_{ZX}}\left\|\tilde{\boldsymbol{U}}\boldsymbol{m}_{ZX}\right\|^2\text{s.t.}\|\boldsymbol{m}_{ZX}\|^2=9. \tag{43}$$

Note that the above equality constraint is a necessary condition for an orthogonality matrix. Using Lagrange multiplier method, the optimization problem is transformed into an unconstrained optimization problem

$$\begin{aligned}L\left(\boldsymbol{m}_{ZX},\lambda\right)&=\left\|\tilde{\boldsymbol{U}}\boldsymbol{m}_{ZX}\right\|^2+\lambda\left(9-\|\boldsymbol{m}_{ZX}\|^2\right)\\&=\boldsymbol{m}_{ZX}^{\mathrm{T}}\tilde{\boldsymbol{U}}^{\mathrm{T}}\tilde{\boldsymbol{U}}\boldsymbol{m}_{ZX}+\lambda\left(9-\boldsymbol{m}_{ZX}^{\mathrm{T}}\boldsymbol{m}_{ZX}\right).\end{aligned} \tag{44}$$

By further using the least squares method, solving the minimum of $\|\tilde{\boldsymbol{U}}\boldsymbol{m}_{ZX}\|^2$ transformed into discovering calculating the unit eigenvector $\sigma_n(\tilde{\boldsymbol{U}}^{\mathrm{T}}\tilde{\boldsymbol{U}})$ corresponding to the minimum eigenvalue of matrix $\tilde{\boldsymbol{U}}^{\mathrm{T}}\tilde{\boldsymbol{U}}$. In accordance with the equality constraint in (43), the solution is equal to three times the unit eigenvector $\sigma_n(\tilde{\boldsymbol{U}}^{\mathrm{T}}\tilde{\boldsymbol{U}})$. Then, $\boldsymbol{M}_{ZX}$ can be obtained by applying the inverse vectorization operator unvec($\bullet$)

$$\boldsymbol{M}_{ZX}=\boldsymbol{R}_Z\otimes\boldsymbol{R}_X=\text{unvec}\left(3\sigma_n\left(\tilde{\boldsymbol{U}}^{\mathrm{T}}\tilde{\boldsymbol{U}}\right)\right). \tag{45}$$

Once $\boldsymbol{R}_Z\otimes\boldsymbol{R}_X$ is determined, the rotational component $\boldsymbol{R}_Y$ can be solved. Equation (29) can be rewritten as follows:

$$\boldsymbol{R}_A^{-1}\boldsymbol{R}_Y\boldsymbol{R}_C=\boldsymbol{R}_X\boldsymbol{R}_B\boldsymbol{R}_Z^{-1}. \tag{46}$$

Applying vectorization operator vec(.) to both sides of (46)

$$\left(\boldsymbol{R}_C^{\mathrm{T}}\otimes\boldsymbol{R}_A^{\mathrm{T}}\right)\text{vec}\left(\boldsymbol{R}_Y\right)=\left(\boldsymbol{R}_Z\otimes\boldsymbol{R}_X\right)\text{vec}\left(\boldsymbol{R}_B\right). \tag{47}$$

Let $\boldsymbol{M}_{CA}=\boldsymbol{R}_C\otimes\boldsymbol{R}_A$, $\boldsymbol{m}_Y=\text{vec}(\boldsymbol{R}_Y)$, and $\boldsymbol{m}_{ZXB}=(\boldsymbol{R}_Z\otimes\boldsymbol{R}_X)\text{vec}(\boldsymbol{R}_B)$, (47) is expressed as a nonhomogeneous linear system

$$\boldsymbol{M}_{CA}^{\mathrm{T}}\boldsymbol{m}_Y=\boldsymbol{m}_{ZXB}. \tag{48}$$

The solutions to $\boldsymbol{m}_Y$ can be determined by least square method

$$\boldsymbol{m}_Y=\left(\boldsymbol{M}_{CA}\boldsymbol{M}_{CA}^{\mathrm{T}}\right)^{-1}\boldsymbol{M}_{CA}\boldsymbol{m}_{ZXB}. \tag{49}$$

The rotational components $\boldsymbol{R}_Y$ can be determined by applying unvec($\boldsymbol{m}_Y$). Note that the solution of $\boldsymbol{R}_Y$ solved by (46) should satisfy rank($\boldsymbol{R}_Y$) >0.

B. Solution for Rotational Components $\boldsymbol{R}_X$, $\boldsymbol{R}_Z$ and Translational Components $\boldsymbol{t}_X$, $\boldsymbol{t}_Y$, $\boldsymbol{t}_Z$

Once the rotational components $\boldsymbol{R}_Y$ is solved, the remaining five unknown components can be simultaneously solved linearly. Equation (29) can be reformulated to solve for the unknown rotational components $\boldsymbol{R}_X$ and $\boldsymbol{R}_Z$

$$\boldsymbol{R}_X\boldsymbol{R}_B=\boldsymbol{R}_A^{-1}\boldsymbol{R}_Y\boldsymbol{R}_C\boldsymbol{R}_Z. \tag{50}$$

The vectorization operator vec($\bullet$) is used to linearize unknown rotational components $\boldsymbol{R}_X$ and $\boldsymbol{R}_Z$

$$\left(\boldsymbol{R}_B^{\mathrm{T}}\otimes\boldsymbol{I}_3\right)\text{vec}\left(\boldsymbol{R}_X\right)=\left(\boldsymbol{I}_3\otimes\left(\boldsymbol{R}_A^{-1}\boldsymbol{R}_Y\boldsymbol{R}_C\right)\right)\text{vec}\left(\boldsymbol{R}_Z\right). \tag{51}$$

In addition, (30) pertaining to unknown translational components $\boldsymbol{t}_X$, $\boldsymbol{t}_Y$, and $\boldsymbol{t}_Z$ can be reformulated as follows:

$$\begin{aligned}&\boldsymbol{R}_Y^{-1}\boldsymbol{R}_A\boldsymbol{R}_X\boldsymbol{t}_B+\boldsymbol{R}_Y^{-1}\boldsymbol{R}_A\boldsymbol{t}_X-\boldsymbol{R}_Y^{-1}\boldsymbol{t}_Y-\boldsymbol{R}_C\boldsymbol{t}_Z\\&=-\boldsymbol{R}_Y^{-1}\boldsymbol{t}_A+\boldsymbol{t}_C.\end{aligned} \tag{52}$$

Authorized licensed use limited to: Shaanxi Normal University. Downloaded on August 06,2024 at 10:57:59 UTC from IEEE Xplore. Restrictions apply.

The vectorization operator vec(•) is utilized once again to linearize $\boldsymbol{t}_X$, $\boldsymbol{t}_Y$, and $\boldsymbol{t}_Z$. Equation (30) can be reformulated as follows:

$$\begin{aligned}&\left(\boldsymbol{t}_B^{\mathrm{T}} \otimes \left(\boldsymbol{R}_Y^{-1}\boldsymbol{R}_A\right)\right) \mathrm{vec}\left(\boldsymbol{R}_X\right) + \boldsymbol{R}_Y^{-1}\boldsymbol{R}_A\boldsymbol{t}_X \\ &-\boldsymbol{R}_Y^{-1}\boldsymbol{t}_Y - \boldsymbol{R}_C\boldsymbol{t}_Z = -\boldsymbol{R}_Y^{-1}\boldsymbol{t}_A + \boldsymbol{t}_C.\end{aligned} \tag{53}$$

Let $\boldsymbol{m}_X = \mathrm{vec}(\boldsymbol{R}_X)$ and $\boldsymbol{m}_Z = \mathrm{vec}(\boldsymbol{R}_Z)$, combining (51) and (52), a system of linear equations can be derived for $\boldsymbol{R}_X$, $\boldsymbol{R}_Z$, $\boldsymbol{t}_X$, $\boldsymbol{t}_Y$, and $\boldsymbol{t}_Z$

Equation (54) shown at the bottom of this page represents a nonhomogeneous linear system. To calculate the values of $\boldsymbol{m}_X$, $\boldsymbol{m}_Z$, $\boldsymbol{t}_X$, $\boldsymbol{t}_Y$, and $\boldsymbol{t}_Z$ the least square method can be employed. Furthermore, the inverse vectorization operator unvec(.) can be used to calculate the rotational components $\boldsymbol{R}_X$ and $\boldsymbol{R}_Z$. Due to noise, the vectorization process employed may lead to the rotations not being strictly orthogonal. If the results from the initial calibration method are being utilized as calibration parameters, reorthogonalization for rotations is necessary. Several orthogonalization methods have been studied for the rotation orthogonalization of hand-eye calibration, such as Rodrigues' rotation formula [18], SVD [21], Gram-Schmidt [40], etc.

In dual-robot calibration, there are three unknown rigid transformations to be determined. The proposed closed-form method for initial calibration method achieves the simultaneous solving of most unknown matrices as much as possible, with only $\boldsymbol{R}_Y$ being solved independently. Compared to existing closed-form method [37] of rotation and translation, the simultaneous solving of most unknown components can reduce the propagation of errors. Due to the sensitivity to noise, closed-form solution methods are often used to calculate the initial calibration results as a basis for subsequent accuracy calibration and parameter settings in the practical calibration process.

C. Pseudocode of the Proposed Method

Combining the accurate calibration method presented in Section II and the initial calibration procedure discussed in Sections III-A and III-B, the complete processes of the proposed dual-robot calibration method are presented in Tables I and II.

TABLE I
PSEUDOCODE OF THE PROPOSED INITIAL DUAL-ROBOT CALIBRATION METHOD

Algorithm 1 The proposed initial dual-robot calibration method	

Input: A_1, A_2, … , A_n ;// The sensor robot's end-effector pose, expressed in its' base frame
B_1, B_2, … , B_n ;// The target' pose, expressed in the sensor frame
C_1, C_2, … , C_n ;// The target robot's end-effector pose, expressed in its' base frame
Output: X_0, Y_0, Z_0 ; // Initial calibration results	

1	Separate the rotation and translation equations based on Eq.(29) and Eq. (30)
2	Compute relative changes $\boldsymbol{R}_{A_{jk}}$ and $\boldsymbol{R}_{C_{jk}}$ of two robot end-flange frame based on Eq.(33)
3	Compute rotation equations after the first-step vectorization based on Eq.(36)
4	Compute homogeneous linear equations about $\boldsymbol{m}_{ZX}$ after the second-step vectorization based on Eq.(39)
5	Compute $\boldsymbol{m}_Y$ based on Eq.(45)-(49)
6	Compute $\boldsymbol{R}_Y$ using inverse vectorization
7	Compute nonhomogeneous linear equations about $\boldsymbol{m}_X$, $\boldsymbol{m}_Z$, $\boldsymbol{t}_X$, $\boldsymbol{t}_Y$ and $\boldsymbol{t}_Z$ based on Eq.(54)
8	Compute $\boldsymbol{R}_X$ and $\boldsymbol{R}_Z$ using inverse vectorization
9	Compute initial calibration results $\boldsymbol{X}_0$, $\boldsymbol{Y}_0$, $\boldsymbol{Z}_0$

IV. EXPERIMENTAL RESULT

A. Simulated Calibration Experiments

1) Simulation System Setup: In the simulation experiments, a dual-robot system is constructed using two KUKA KR16 R1610 robots, as shown in Fig. 2. Kinematics parameters for the robots are obtained from the manufacturer's user manual. The nominal values for the unknown transformation $\boldsymbol{X}$, $\boldsymbol{Y}$, and $\boldsymbol{Z}$ can be found in Table III. The length units of translational components in the simulated calibration experiments are in millimeters. These nominal twist values provide the baseline standards used to evaluate and optimize the robotic system.

2) Simulation Data Generation: The matrices $\boldsymbol{A}$ and $\boldsymbol{C}$ are generated simultaneously by placing the sensor robot and target robot in a random configuration within their respective workspaces. Additionally, the rotation matrices of all generated data must meet the solvability conditions outlined in [34] and [37]. Using the robot forward kinematics model, the experiments can generate $n(n = 100, 200, \ldots, 1000)$ sets of simulation robot data $\boldsymbol{A}_i(i = 1, 2, \ldots, n)$ and $\boldsymbol{C}_i(i = 1, 2, \ldots, n)$. All generated robot data are restricted by the joint angle ranges to ensure they are within the robot's valid workspace. The simulation measurement data $\boldsymbol{B}_i(i = 1, 2, \ldots, n)$ can be calculated by $\boldsymbol{B}_i = (\boldsymbol{A}_i\boldsymbol{X})^{-1}\boldsymbol{Y}\boldsymbol{C}_i\boldsymbol{Z}$. To simulate actual calibration, noise at varying levels is introduced to the ideal simulation data, acting as a small perturbation. The perturbation, denoted as $\delta\boldsymbol{\xi}_p$, can is expressed as a twist of $se(3)$. The perturbation consists of a twist $\delta\boldsymbol{\phi}_p = [\delta\phi_x \quad \delta\phi_y \quad \delta\phi_z]^{\mathrm{T}}$ associated with its rotation and a vector $\delta\boldsymbol{\rho}_p = [\delta\rho_x \quad \delta\rho_y \quad \delta\rho_z]^{\mathrm{T}}$ associated with its translation. The perturbations for different levels of noise are shown in

$$\begin{bmatrix} \boldsymbol{R}_B^{\mathrm{T}} \otimes \boldsymbol{I}_3 & -\boldsymbol{I}_3 \otimes \left(\boldsymbol{R}_A^{-1}\boldsymbol{R}_Y\boldsymbol{R}_C\right) & \boldsymbol{0} & \boldsymbol{0} & \boldsymbol{0} \\ \boldsymbol{t}_B^{\mathrm{T}} \otimes \left(\boldsymbol{R}_Y^{-1}\boldsymbol{R}_A\right) & \boldsymbol{0} & \boldsymbol{R}_Y^{-1}\boldsymbol{R}_A & -\boldsymbol{R}_Y^{-1} & -\boldsymbol{R}_C \end{bmatrix} \begin{bmatrix} \boldsymbol{m}_X \\ \boldsymbol{m}_Z \\ \boldsymbol{t}_X \\ \boldsymbol{t}_Y \\ \boldsymbol{t}_Z \end{bmatrix} = \begin{bmatrix} \boldsymbol{0} \\ -\boldsymbol{R}_Y^{-1}\boldsymbol{t}_A + \boldsymbol{t}_C \end{bmatrix}. \tag{54}$$

Authorized licensed use limited to: Shaanxi Normal University. Downloaded on August 06,2024 at 10:57:59 UTC from IEEE Xplore. Restrictions apply.

TABLE II
PSEUDOCODE OF THE PROPOSED ACCURATE DUAL-ROBOT CALIBRATION METHOD

Algorithm 2 The proposed accurate dual-robot calibration method

Input: $\boldsymbol{A}_1, \boldsymbol{A}_2, \ldots, \boldsymbol{A}_n$;// The sensor robot's end-effector pose, expressed in its' base frame
$\boldsymbol{B}_1, \boldsymbol{B}_2, \ldots, \boldsymbol{B}_n$;// The target' pose, expressed in the sensor frame
$\boldsymbol{C}_1, \boldsymbol{C}_2, \ldots, \boldsymbol{C}_n$;// The target robot's end-effector pose, expressed in its' base frame
$\boldsymbol{X}_0, \boldsymbol{Y}_0, \boldsymbol{Z}_0$; // Initial calibration results

Output: $\boldsymbol{X}, \boldsymbol{Y}, \boldsymbol{Z}$; // Accurate calibration results

Initialization: *MaxIters*, *iter*←0
Convert calibration data into Lie algebra representation $\boldsymbol{\xi}_A$, $\boldsymbol{\xi}_B$ and $\boldsymbol{\xi}_C$
Compute iterative initial values $\boldsymbol{\xi}_{X_0}$, $\boldsymbol{\xi}_{Y_0}$ and $\boldsymbol{\xi}_{Z_0}$ based on initial calibration results
Compute weight coefficient w_ρ and w_ϕ based on Eq.(25)-(26)
Compute the scaling twists $\boldsymbol{\xi}'_A$, $\boldsymbol{\xi}'_B$, $\boldsymbol{\xi}'_C$, $\boldsymbol{\xi}'_{X_0}$, $\boldsymbol{\xi}'_{Y_0}$, and $\boldsymbol{\xi}'_{Z_0}$
while(*iter*<*MaxIters*)
  Compute transformation chain $\boldsymbol{g}_a$ using the scaling twists based on Eq.(7)
  Compute transformation deviation $\ln(\boldsymbol{e})$ based on Eq.(8)
  Compute Jacobian matrix $\boldsymbol{J}_{XYZ}$ based on Eq.(16)-(18)
  Compute optimal perturbation $\delta\boldsymbol{\xi}^*_{XYZ_{op}}$ based on the Newton-like methods
  Update optimization objectives based on Eq.(22)-(24)
  iter←*iter*+1
until $\delta\boldsymbol{\xi}^*_{XYZ_{op}}$ is small enough
Correct magnitude of optimization objectives after scaling based on Eq.(28)
Compute calibration results $\boldsymbol{X}$, $\boldsymbol{Y}$, $\boldsymbol{Z}$ based on exponential map

TABLE III
NOMINAL TWIST VALUE FOR THE UNKNOWN TRANSFORMATION IN THE SIMULATION DUAL-ROBOT CALIBRATION EXPERIMENTS

Unknown	Nominal value of $\boldsymbol{\rho}$	Nominal value of $\boldsymbol{\phi}$	Nominal Rigid Transformation
$\boldsymbol{X}$	$\begin{bmatrix}150\\150\\150\end{bmatrix}$	$\begin{bmatrix}0.2\\0.2\\0.2\end{bmatrix}$	$\begin{bmatrix}0.9604 & -0.1762 & 0.2158 & 150.0000\\ 0.2158 & 0.9604 & -0.1762 & 150.0000\\ -0.1762 & 0.2158 & 0.9604 & 150.0000\\ 0 & 0 & 0 & 1\end{bmatrix}$
$\boldsymbol{Y}$	$\begin{bmatrix}1000\\0\\0\end{bmatrix}$	$\begin{bmatrix}0.5\\0.3\\0.1\end{bmatrix}$	$\begin{bmatrix}0.9514 & -0.0214 & 0.3071 & 983.6226\\ 0.1671 & 0.8737 & -0.4568 & 73.1247\\ -0.2585 & 0.4859 & 0.8349 & -137.4870\\ 0 & 0 & 0 & 1\end{bmatrix}$
$\boldsymbol{Z}$	$\begin{bmatrix}-100\\-100\\-100\end{bmatrix}$	$\begin{bmatrix}0.1\\0.3\\0.5\end{bmatrix}$	$\begin{bmatrix}0.8349 & -0.4568 & 0.3071 & -86.0302\\ 0.4859 & 0.8737 & -0.0214 & -118.1132\\ -0.2585 & 0.1671 & 0.9514 & -91.9260\\ 0 & 0 & 0 & 1\end{bmatrix}$

Table IV. The corresponding rigid transformation $\delta\boldsymbol{T}_p$ can be obtained using exponential map

$$\delta\boldsymbol{T}_p = \exp\left(\delta\hat{\boldsymbol{\xi}}_p\right). \tag{55}$$

To generate twists associated with perturbation for different noise levels, a random number function with distribution $U(l,u)$ is used, where l and u indicate the lower and upper bounds, respectively. The simulation experiments comprise three different noise levels, which are labeled as "low," "medium," and "high" which are indicated in Table II. In these experiments, the noise is injected into simulation data by left multiplying

$$\boldsymbol{T'}_i = \delta\boldsymbol{T}_p\boldsymbol{T}_i \tag{56}$$

where $\boldsymbol{T'}_i$ represents the simulation data with the noise.

TABLE IV
INJECTION OF NOISE AT DIFFERENT LEVELS INTO SIMULATION DATA

Noise level	Rotational noise	Translational noise
Low	$\delta\phi_x, \delta\phi_y, \delta\phi_z$: $U(-0.01, 0.01)$	$\delta\rho_x, \delta\rho_y, \delta\rho_z$: $U(-0.1, 0.1)$
Medium	$\delta\phi_x, \delta\phi_y, \delta\phi_z$: $U(-0.03, 0.03)$	$\delta\rho_x, \delta\rho_y, \delta\rho_z$: $U(-0.5, 0.5)$
High	$\delta\phi_x, \delta\phi_y, \delta\phi_z$: $U(-0.05, 0.05)$	$\delta\rho_x, \delta\rho_y, \delta\rho_z$: $U(-1, 1)$

3) Experiment on Different Number of Samples: The errors of rotational and translational components of the simulation experiments are defined as follows:

$$e_{\boldsymbol{R}} = \left\|\ln\left(\boldsymbol{R}_n\tilde{\boldsymbol{R}}^{\mathrm{T}}\right)\right\| \tag{57}$$

$$e_{\boldsymbol{t}} = \left\|\boldsymbol{t}_n - \tilde{\boldsymbol{t}}\right\| \tag{58}$$

where $\boldsymbol{R}_n$ is the nominal rotation matrix, $\tilde{\boldsymbol{R}}$ is the solved rotation matrix, $\boldsymbol{t}_n$ represents the nominal translation vector, and $\tilde{\boldsymbol{t}}$ represents the solved translation vector. Four methods are used in the simulation experiments, including the proposed initial calibration, the proposed accurate method, Wu's method [34] and Wang's method [37]. Wu's method solves the rotational components of unknown transformation matrices through nonlinear iteration, and the translational components can then be solved. In contrast, Wang's method solves the rotational and translational components of unknown matrices simultaneously through nonlinear iteration. In order to control the variables in the experiment, the proposed accurate calibration method, Wang's method, and Wu's method all use the same initial values calculated using the proposed initial calibration method in Section III.

The experiment results are presented in Figs. 3–5. These results show that the proposed accurate method has significantly lower rotation errors for $\boldsymbol{R}_X$ and $\boldsymbol{R}_Z$ than Wu's method and Wang's method. However, the errors for rotation $\boldsymbol{R}_Y$ appear to be consistent across all methods. This is because the initial solution for $\boldsymbol{R}_Y$ establishes a minimum optimization problem surrounding an intermediate variable in Section III-A, resulting in a relatively high initial calibration accuracy of $\boldsymbol{R}_Y$. Furthermore, since the initial calibration result of $\boldsymbol{R}_Y$ is calculated separately, its calculation process can ensure that the calculation results meet the relevant constraints of $\boldsymbol{R}_Y$. Consequently, using the results calculated by the proposed initial calibration method as the initial value of the optimization variable about $\boldsymbol{R}_Y$, the postconvergence error reduction is insignificant. For the translational components $\boldsymbol{t}_X$, $\boldsymbol{t}_Y$, and $\boldsymbol{t}_Z$, the proposed

Authorized licensed use limited to: Shaanxi Normal University. Downloaded on August 06,2024 at 10:57:59 UTC from IEEE Xplore. Restrictions apply.

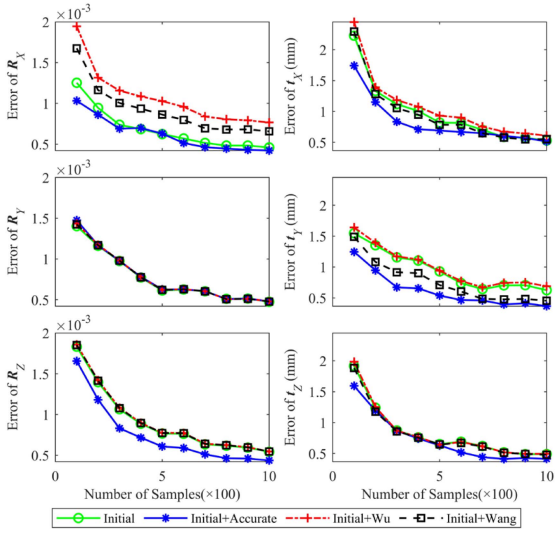

Fig. 3. Average accuracy of four methods under low-level noise with varying sample sizes.

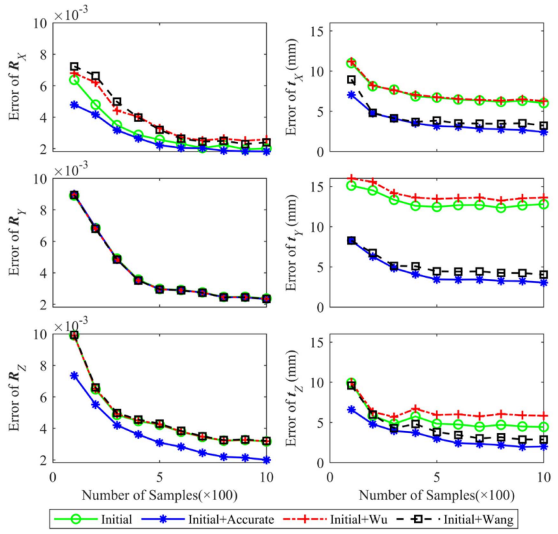

Fig. 5. Average accuracy of four methods under high-level noise with varying sample sizes.

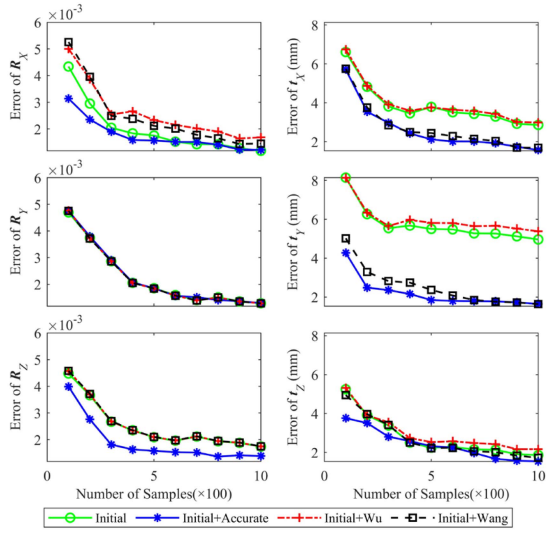

Fig. 4. Average accuracy of four methods under middle-level noise with varying sample sizes.

accurate method produces better calibration results than the other methods. Furthermore, it appears that the translational calibration accuracy of the proposed accurate method is more prominent with increasing noise levels. Additionally, in certain cases, such as for $\boldsymbol{R}_X$, the rotational errors of the proposed initial calibration method are smaller than those for Wu's and Wang's methods. Finally, increasing the sample size leads to a reduction in the errors of both rotational and translational components, thereby mitigating the impact of noise.

The errors in Wu's method are larger than those in the accurate calibration method proposed in this study and Wang's method. This is because Wu's method directly estimates errors of the rotations using a first-order approximation, which introduces a truncation error. Additionally, Wu's method requires the least square method to solve the translations after solving the unknown rotation matrices. The separate solving of rotations and translations can lead to error propagation. In contrast, the optimization model proposed in this study fully constrains all unknowns and solves both the translations and rotations simultaneously, avoiding error propagation. In most cases, Wang's method produces larger errors than the accurate calibration method proposed in this study. Wang's method builds residual error items using (29) and (30), and adds penalty terms to ensure orthogonality of the rotations. Because the terms in the objective function have different weight coefficients, Wang's model is not a quadratic form and needs to be solved using the SVRG method, an adaptation of the gradient descent method that introduces additional hyperparameters based on experience. With inappropriate parameters, Wang's method may produce a suboptimal result. In contrast, our method's quadratic form ensures convergence of the optimal result, and the Jacobian matrix of the objective function is explicitly derived by Lie derivative. The optimal result can be easily determined using Gauss–Newton iterative methods without additional parameters.

4) Experiment on Different Number of Iterations: To compare errors with different numbers of iterations, the proposed accurate calibration methods are compared with Wu's and Wang's methods. For each method, varying numbers of iterations ranging from 0 to 200 were used, and 200 sets of simulation data with medium noise levels were calculated using each respective method. In the experiment, the proposed accurate calibration method, Wang's method, and Wu's method all use the same initial values calculated using the proposed initial calibration method in Section III. Each method's experiment was repeated 10 times, and their average errors were calculated.

The experiment results, shown in Fig. 6, demonstrate that the errors of both rotations and translations in the proposed accurate calibration method after convergence are smaller than those in Wu's and Wang's methods. The convergent iteration number of our method is comparable with Wu's and Wang's methods. However, the errors of Wu's method show obvious fluctuation after convergence due to the truncation error introduced by

Authorized licensed use limited to: Shaanxi Normal University. Downloaded on August 06,2024 at 10:57:59 UTC from IEEE Xplore. Restrictions apply.

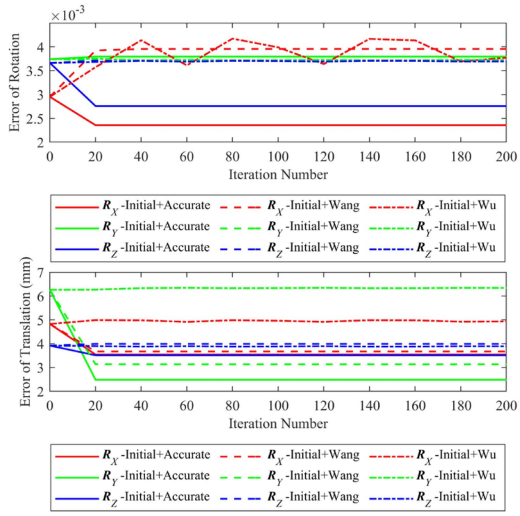

Fig. 6. Average accuracy for the proposed accurate calibration method, Wang's method, and Wu's method under different numbers of iterations.

TABLE V
CALCULATION ERRORS OF DIFFERENT METHODS WITHOUT INITIAL VALUES AND INITIAL CALIBRATION VALUES

Method with different initial value		Rotational Error			Translational Error (mm)		
		R_X	R_Y	R_Z	t_X	t_Y	t_Z
Proposed method	A	0.0024	0.0037	0.0027	3.5426	2.4844	3.5107
	B	0.0024	0.0037	0.0027	3.5426	2.4844	3.5107
Wu's method	A	0.0870	0.0589	0.0588	27.7350	53.1122	10.0764
	B	0.0044	0.0037	0.0037	5.0086	6.3265	3.8679
Wang's method	A	0.0040	0.0037	0.0037	3.6730	3.1315	3.9906
	B	0.0040	0.0037	0.0037	3.6730	3.1315	3.9906
	C	0.0039	0.0037	0.0037	4.9181	6.6787	3.9300
	D	0.0039	0.0037	0.0037	4.4179	5.1063	3.8940

the first-order approximation in the optimization process. In contrast, the smoothness of the Lie algebra and the convergence of the quadratic form ensure that the proposed method's errors remain stable during iteration.

5) Experiment on Initial Value Fluctuations: In order to evaluate the influence of different initial value fluctuations on the calculated results of the proposed optimization method, two types of initial values were used in the experiment. One type uses the identity matrix directly as the initial value, and the other type adds perturbation to the initial value calculated through the proposed initial calibration method. The experiment also used Wu's method and Wang's method as comparisons at the same time.

In the experiment using the identity matrix as the initial value, the experiment used 200 groups of samples with medium-level noise and set the number of iterations to 100. The identity matrix and the initial calibration result calculated by Section III are used as initial values of iterative calculation, respectively. The calibration errors are shown in Table V. The initial values for group A in the table are the identity matrix, while the initial values for group B are the initial calibration results. Groups C and D of Wang's method are calibration errors obtained after slightly adjusting the weight values of the residual error terms corresponding to the rotation part and translation part, respectively. Experimental results show that the proposed optimization model can converge

TABLE VI
OPTIMIZATION RESULTS OF DIFFERENT WEIGHTING COEFFICIENTS

Weight coefficients	Error of rotation			Error of translation (mm)		
	R_X	R_Y	R_Z	t_X	t_Y	t_Z
1	0.0030	0.0064	0.0029	3.7326	5.7750	3.4828
200	0.0028	0.0038	0.0029	3.7005	2.4899	3.4835
400	0.0026	0.0038	0.0029	3.6335	2.5082	3.4865
600	0.0024	0.0038	0.0028	3.5729	2.5003	3.4928
800	0.0023	0.0038	0.0028	3.5439	2.4901	3.5027
929.53	**0.0024**	**0.0037**	**0.0027**	**3.5426**	**2.4844**	**3.5107**
1000	0.0024	0.0037	0.0028	3.5469	2.4816	3.5152
1200	0.0026	0.0037	0.0028	3.5689	2.4756	3.5290
1400	0.0027	0.0037	0.0029	3.5984	2.4716	3.5428
1600	0.0029	0.0037	0.0029	3.6287	2.4691	3.5558
1800	0.0030	0.0037	0.0030	3.6569	2.4676	3.5678
2000	0.0031	0.0037	0.0031	3.6819	2.4668	3.5784

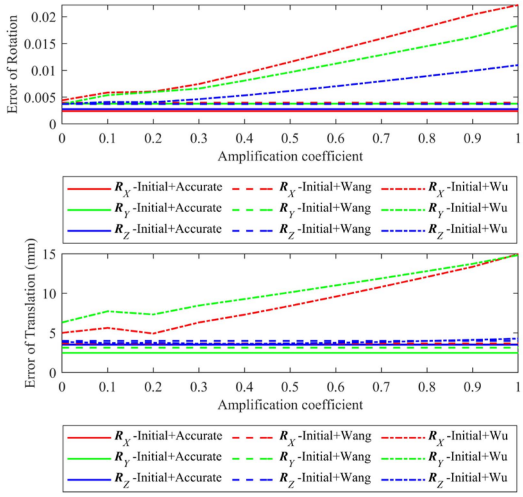

Fig. 7. Average error for the proposed accurate calibration method, Wang's method, and Wu's method under different initial values.

stably, Wu's method [34] is relatively sensitive to initial values, and Wang's method [37] can also converge as long as the weight coefficients of residual error settings are reasonable. However, once the weight coefficients of residual error items are set improperly, the calibration accuracy of Wang's method will decrease.

Additionally, different perturbations were introduced into the initial values in the experiment. The initial perturbed values were calculated by left-multiplying as follows:

$$\boldsymbol{T}'_0 = \exp\left(\delta\boldsymbol{\xi} \cdot a\right) \boldsymbol{T}_0 \tag{59}$$

where $\boldsymbol{T}_0$ is the initial value without perturbation, $\delta\boldsymbol{\xi}$ represents the perturbation expressed as an element of $se(3)$ using a twist representation, and a represents the amplification coefficient. The initial values $\boldsymbol{T}_0$ for the three methods compared in the experiment all use the same initial values obtained by the proposed initial calibration method in Section III. The twist $\delta\boldsymbol{\xi}$ are generated using a uniform distribution $U(-0.1, 0.1)$. The amplification coefficient a increases from 0 to 1 in steps of 0.1. The experiment is repeated 10 times for each amplification coefficient and calculate the average errors for different initial values.

Authorized licensed use limited to: Shaanxi Normal University. Downloaded on August 06,2024 at 10:57:59 UTC from IEEE Xplore. Restrictions apply.

The result, shown in Fig. 7, demonstrates that the errors of rotations and translations in the proposed accurate calibration method and Wang's method are not significantly affected by fluctuations in initial values. In contrast, Wu's method shows an increase in rotational and translational errors with added perturbations to the initial values due to truncation error introduced by the first-order approximation used in the optimization process. Wang's method can obtain relatively stable iteration results by reasonably setting the weight coefficients of each error term in the objective function. The proposed convex optimization model has good convergence in the vicinity of reasonable initial values, so it also has better tolerance for the selection of initial values.

6) Experiment on Different Weighting Coefficient for the Proposed Accurate Calibration: The experiment aimed to validate the effectiveness and rationality of the weighting coefficient calculation method introduced in Section II-B. The experiment used 200 sets of groups of samples with medium-level noise, with 100 iterations and varying weight coefficients $\frac{w_t}{w_R}$ ranging from 1 to 2000. The unit of the translation variable in the experiment is millimeters. The rotational and translational variables are not weighted when the weight coefficient equals 1. Table VI indicates the discrepancy in optimization results of different weighting coefficients. As the weight coefficient increased, the magnitude of the translational variables decreased, and vice versa. The results showed a nonmonotonic relationship between weight coefficients and errors of variables $\boldsymbol{R}_X$, $\boldsymbol{R}_Z$, $\boldsymbol{t}_X$, and $\boldsymbol{t}_Z$. These errors were minimized when the weight coefficient was between 800 to 1000, and the weight coefficients corresponding to the minimum error can be found in the bold values of Table VI. On the other hand, $\boldsymbol{R}_Y$ and $\boldsymbol{t}_Y$ errors rapidly decreased at the beginning of weight coefficient increase up to 200, but reductions in errors became less significant beyond this point. Using the method proposed in Section II-B, the calculated weight coefficient was 929.53, which falls within the appropriate range. These results indicate that the use of weighting coefficients proposed in Section II-B is appropriate, as it balances the contributions of optimization variables to the objective function, ensuring that the errors of these variables converge to the desired values.

B. Actual Calibration Experiments

In addition to simulated experiments, actual experimental calibrations were performed on a dual-robot experiment platform, as depicted in Fig. 8. The platform comprises two distinct industrial robots. The first robot (ABB IRB 1600 10/1.45, 6 DOFs, pose repeatability 0.07 mm) is equipped with a PowerScan Pro 2.3M 3D scanner (accuracy of measurement ±0.015 mm, reference measuring distance of 500 mm). The second robot (ABB IRB 6700 200/2.60, 6 DOFs, pose repeatability 0.10 mm) is fitted with a F120 Jäger spindle (maximum rotation speed 24000 rpm, rated power 24 kW) and an end-effector with a 3-D calibration target. Thus, this experimental setup provides a reliable means of evaluating the proposed calibration method.

In the experiment, a 3-D calibration target comprised of four ceramic spheres was used to establish the tool coordinate systems of the target robot, as illustrated in Fig. 9. The calibration target is composed of four ceramic spheres S1, S2, S3, and S4. The spheres S2 and S3 form a sphere-bar, which has a fixed distance between the centers of the two balls. The centers of the S1 sphere and the sphere-bar are used to establish the target coordinate system. The calibration target's ceramic spheres are certified by coordinate measuring machine, the results of which are presented in Table VII.

A 3-D calibration target is mounted on ABB IRB 6700 robot. The calibration target is scanned using a 3-D scanner to capture a point cloud. During the experiment, the matrices $\boldsymbol{A}$ and $\boldsymbol{C}$ can are read simultaneously from the robot controllers, and the corresponding matrices $\boldsymbol{B}$ are obtained using the 3-D scanner's measuring data. The length units of translational components in the calibration data $\boldsymbol{A}$, $\boldsymbol{B}$, and $\boldsymbol{C}$ are in millimeters. The tool coordinate systems of the experiment platform are established based on the actual assembly relationship to generate sample data needed for the calibration experiment. The tool center point (TCP) of the sensor robot is placed at the 3-D scanner's reference measuring point, and that of the target robot is positioned at the

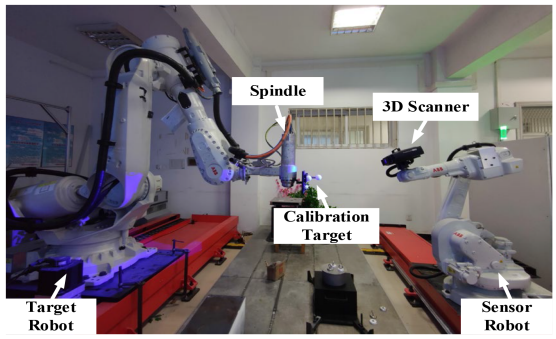

Fig. 8. Practical experiments are carried out with an ABB IRB 6700 200/2.60 robot equipped with a three-dimensional calibration target and an ABB IRB 1600 10/1.45 robot equipped with a PowerScan Pro-5M 3-D scanner.

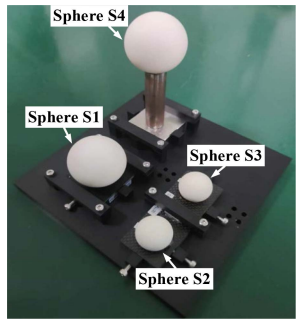

Fig. 9. 3-D calibration target is composed of two ceramic spheres and a ceramic sphere-bar, and the coordinate system is established by the centers of ceramic sphere S1 and ceramic sphere-bar.

TABLE VII
CERTIFIED RESULTS OF THE STANDARD CERAMIC SPHERES AND CERAMIC SPHERE-BAR USED IN EXPERIMENTS

	Diameter (mm)	Center distance (mm)
Sphere S1	50.7980	——
Sphere S2	30.0018	60.0865
Sphere S3	29.9968	
Sphere S4	50.8054	——

Authorized licensed use limited to: Shaanxi Normal University. Downloaded on August 06,2024 at 10:57:59 UTC from IEEE Xplore. Restrictions apply.

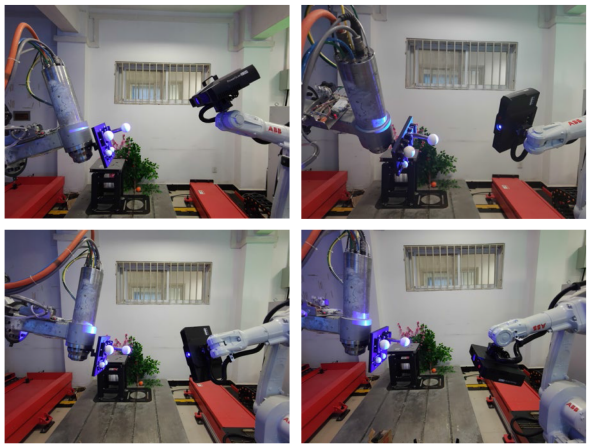

Fig. 10. Attitudes of both end-effector are adjusted so that the base board of the 3-D calibration target faces the 3-D scanner in the experiment.

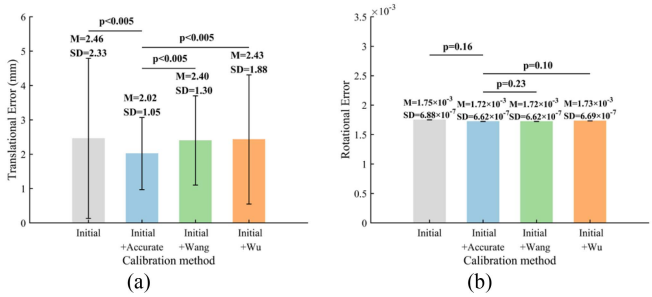

Fig. 11. Mean and the standard deviations of the calibration errors are calculated, and T-test is used to compare the performance of the proposed accurate calibration method with Wang's method and Wu's method. (a) Translational error. (b) Rotational error.

TABLE VIII
CALIBRATION ACCURACY AND ITERATION COMPUTATION TIMES USING DIFFERENT ITERATION INITIAL VALUES

Initial values for iteration	Rotational error	Translational error (mm)	Iteration computation times
Identity matrix	0.0017	2.0187	24
The results obtained by the proposed initial calibration method	0.0017	2.0187	7

original point of the 3-D calibration target. The valid measuring area for the calibration experiment is determined by the intersection of the reachable spaces of the two robots' TCPs. The calibration experiment uses 200 sets of qualified robot attitudes, which are uniformly distributed over the valid measuring area. To ensure measuring accuracy, the 3-D scanner is maintained at a roughly reference measuring distance from the 3-D calibration target, and the attitudes of both end-effectors are adjusted to ensure that the 3-D scanner faces the 3-D calibration target, as illustrated in Fig. 10.

In the absence of a nominal value in the actual calibration experiment, the calibration errors $\boldsymbol{E}_i$ can be defined by transformation chain (3)

$$\boldsymbol{E}_i = \boldsymbol{A}_i \hat{\boldsymbol{X}} \boldsymbol{B}_i \left(\hat{\boldsymbol{Y}} \boldsymbol{C}_i \hat{\boldsymbol{Z}} \right)^{-1} \tag{60}$$

where $\hat{\boldsymbol{X}}$, $\hat{\boldsymbol{Y}}$, and $\hat{\boldsymbol{Z}}$ represent optimization results. The error represents a transformation deviation of different calibration data based on the calibration results and can be separated into rotational and translational components. By expanding the transformation matrix, the error of the rotational and translational components at the ith group of calibration data can be represented as follows:

$$e_{\boldsymbol{R}i} = \left\| \ln \left(\boldsymbol{R}_{A_i} \boldsymbol{R}_X \boldsymbol{R}_{B_i} (\boldsymbol{R}_Y \boldsymbol{R}_{C_i} \boldsymbol{R}_Z)^{-1} \right) \right\| \tag{61}$$

$$e_{\boldsymbol{t}i} = \left\| \begin{matrix} -\boldsymbol{R}_A \boldsymbol{R}_X \boldsymbol{R}_B \boldsymbol{R}_C^{-1} \boldsymbol{R}_Z^{-1} \boldsymbol{R}_Y^{-1} \boldsymbol{t}_Y - \boldsymbol{R}_A \boldsymbol{R}_X \boldsymbol{R}_B \boldsymbol{R}_C^{-1} \boldsymbol{R}_Z^{-1} \boldsymbol{t}_Z \\ -\boldsymbol{R}_A \boldsymbol{R}_X \boldsymbol{R}_B \boldsymbol{R}_C^{-1} \boldsymbol{t}_C + \boldsymbol{R}_A \boldsymbol{R}_X \boldsymbol{t}_B + \boldsymbol{R}_A \boldsymbol{t}_X + \boldsymbol{t}_A \end{matrix} \right\|. \tag{62}$$

During the experiment, 150 sets of sample data were used to determine the unknown matrices, while the remaining 50 sets were used to evaluate the calibration errors. For the purpose of controlling the experimental variables, the proposed accurate calibration method, Wang's method, and Wu's method all employ the initial calibration results obtained from the proposed initial calibration method as the initial values. The weight coefficient $\frac{w_\phi}{w_\rho}$ for the proposed accurate calibration method in the actual calibration process is fixed at 1000, based on the experimental results of the weight coefficients obtained from Section IV-A6. The mean and standard deviations of the calibration errors are calculated, and a T-test is used to compare the performance of the proposed the proposed accurate calibration method with Wang's and Wu's methods. Figs. 10(a) and 11(b) show the results of both the translational and rotational components, respectively. The proposed method has significantly better calibration accuracy than Wang's and Wu's methods for the translational components, with a mean error that is obviously smaller and p-value less than 0.005 in the paired-sampled T-test with 99% confidence level. The rotational components have a mean reprojection error that is close to Wang's method and slightly smaller than Wu's method for the calibration results of the proposed method. This is because the noise error in the actual calibration experiment is close to the low noise level in the simulation experiment, which makes the error of the rotation components relatively small in numerical value. Moreover, both the methods in Wang's method and Wu's method have fully optimized the rotation part in the calibration problem of the dual-robot system, which further makes the difference in the error of the rotation part in the actual calibration results not significant.

To further verify the impact of initial values on the proposed accurate calibration method. the identity matrix and the calculated results of the proposed initial calibration method are used as the initial values for the proposed accurate calibration method in the experiment. The calibration accuracy and iteration computation times for the two types of initial values are shown in Table VIII. The results indicate that when using the calculated results of the proposed initial calibration method as the initial values for iteration, the iteration computation times can be effectively reduced. However, there is no significant difference

Authorized licensed use limited to: Shaanxi Normal University. Downloaded on August 06,2024 at 10:57:59 UTC from IEEE Xplore. Restrictions apply.

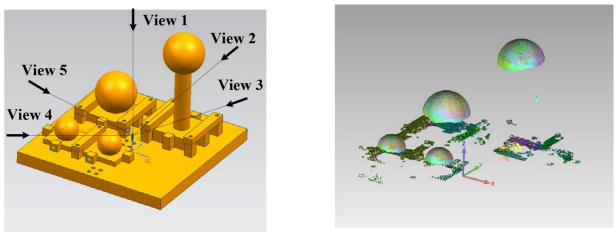

Fig. 12. (a) Measurement system collects the point cloud of the measuring object under five different views. (b) Point cloud of the calibration target under five different views are transformed to the base frame of the target robot.

in the calculation accuracy of the two initial values, which is consistent with the experimental results in Section IV-A5.

Upon completing the calibration, the point clouds collected by the 3-D scanner at different robot attitudes can be merged into a unified coordinate system. As a result, the dual-robot measurement system can be considered a multiview 3-D measurement system, and its accuracy reflects the calibration method's performance. VDI/VDE 2634-3 is a recognized guideline to evaluate the accuracy of multiview 3-D measurement systems based on area scanning for 3-D measurement systems. To evaluate the measurement accuracy of the dual-robot system based on the calibration results, data merge is performed using the ceramic sphere S2 of the calibration target, and the proposed method, Wang's method, and Wu's method are used for calibration. In the experiment, five measuring regions are selected from the valid measuring area of the dual-robot system with uniform distribution. Then, for any one measuring region, the measuring object is kept within the measuring range of the 3-D scanner while changing the attitudes of both robots simultaneously to collect the point cloud of the measuring object under five different views, as shown in Fig. 12(a). The attitudes of both robots used in the calibration should not be used during measurement. The calibration target's point cloud is transformed to the target robot's base frame in five different views, as illustrated in Fig. 12(b). The least-square method is then used to obtain the measured diameter d_m of the ceramic sphere S2. The difference between the measured diameter and certified diameter is defined as the measurement error

$$e_d = |d_c - d_m| . \tag{63}$$

The experiment is repeated five times in different regions within the valid measuring area of the experiment platform. The errors in diameter are presented in Table IX. The mean error of the proposed accurate calibration method is significantly lower than both Wu's and Wang's methods, decreasing by 52.41% and 18.31%, respectively. These results are consistent with those of the simulation experiments.

C. Actual Dual-Robot Collaborative Machining Experiment

Robotic machining is an important application scenario of multirobot systems. Workpiece positioning is an important part of robot machining, especially for complex surface parts lacking

TABLE IX
ERRORS OF THE DIAMETER AFTER CALIBRATION BASED ON WU'S METHOD, WANG'S METHOD AND THE PROPOSED METHOD

	Close method (mm)	Proposed method (mm)	Wang's method (mm)	Wu's method (mm)
1	52.4563	50.0645	50.1393	52.3201
2	52.0372	50.7995	49.9159	52.0569
3	51.0513	50.5227	50.847	51.0256
4	49.9996	51.4048	50.5881	50.0418
5	51.7541	50.2437	49.9384	51.6580
Mean error (mm)	0.9766	0.4381	0.5363	0.9205

Fig. 13. Four types of workpiece sample are selected to be machined, including square plane sample, circular plane sample, curved aircraft skin sample, and cavity sample.

positioning features. It is difficult to determine the posture data of the workpiece through simple alignment methods. In a dual-robot system, the measurement robot can scan the workpiece to be machined through the sensors it carries. The position of the workpiece coordinate system is determined by matching the measured data with the model. Furthermore, through the transformation relationship of the dual-robot system, the position of the workpiece coordinate system is transformed to the base coordinate system of the machining robot. In this study, experiments were conducted on a platform for dual-robot collaborative machining. Four types of aluminum alloy samples were selected for machining, including a square skin sample measuring 200 × 200 mm, a circular skin sample with a 200 mm radius, a curved skin sample measuring 350 × 300 mm, and a cavity sample measuring 100 × 75 × 50 mm, as shown in Fig. 13.

During the experiment, the workpiece is secured in the proper working area, then a 3-D scanner mounted on a sensor robot is utilized to scan and identify the workpiece's location. Point cloud matching and calibration results are used to obtain the actual position of the workpiece in the base frame of the target robot. Due to the numerous conversion steps involved in workpiece positioning and actual machining, such as robot

Authorized licensed use limited to: Shaanxi Normal University. Downloaded on August 06,2024 at 10:57:59 UTC from IEEE Xplore. Restrictions apply.

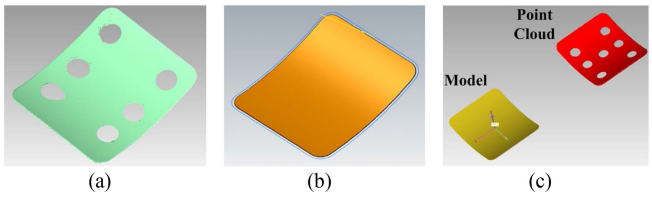

Fig. 14. (a) Point cloud data of the workpiece collected by the sensor robot. (b) Machining trajectory of skin samples generated by the corresponding theoretical contour. (c) Point cloud matching is used to locate the workpiece to be machined.

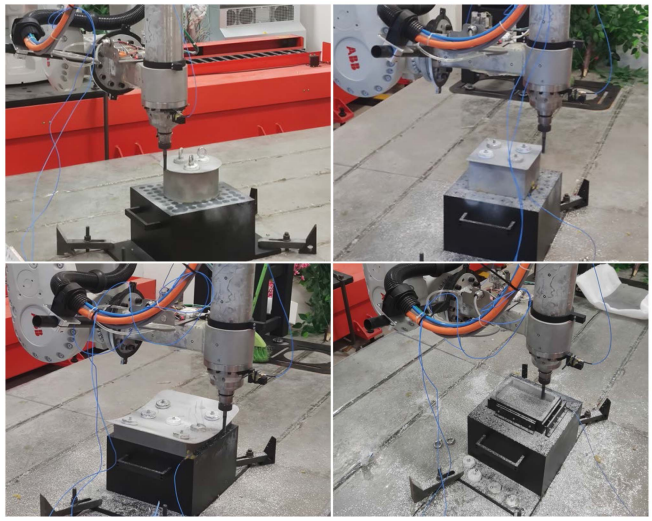

Fig. 15. Robot equipped with machining spindle is used to perform machining task.

kinematic errors, sensor measurement errors, and tool center point calibration errors, the experiment aims to verify the effectiveness of the dual-robot calibration results. Therefore, in the experiment, the measurement data of the sensor robot are mainly used for preliminary positioning of the workpiece. According to the results of Sections IV-A and IV-B, the translation error of the dual-robot system calibration is numerically larger than the rotation error. Before actual machining, robot simulation software and simulated machining are used to make reasonable adjustments to the workpiece position based on the preliminary positioning data. The machining path generated from a model is transformed to correspond to the position of the workpiece, as shown in Fig. 14. As illustrated in Fig. 15, the machining task is carried out using a robot equipped with a machining spindle. The main purpose of machining for aircraft skin is to remove boundary allowance, with the machining allowance for skin samples set at 2.0 mm. For aircraft cavity samples, the machining mainly removes allowance of the inner wall, with the machining allowance set at 1.0 mm. All the samples are machined at a spindle speed of 6000 r/min and a cutting speed of 30 mm/min.

Since both the skin and cavity samples are machined based on their surface profiles, profile tolerance is defined as the allowable variation of a surface's shape from its ideal or nominal form. It is used to ensure that manufactured parts meet specific design

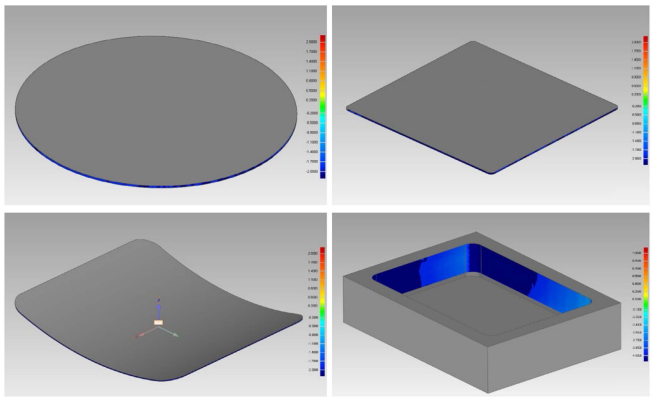

Fig. 16. Machined workpieces are measured again to evaluate material removal.

TABLE X
PROFILE ERRORS OF ALL MACHINED SAMPLES

Type of samples	Mean profile error(mm)
Square skin	0.0804
Circular skin	0.0111
Curved skin	0.2170
Cavity	0.0413

requirements for form, which are critical for proper functionality and assembly. Thus, the quality of the machining in the experiment can be evaluated by profile error that refers to the profile of the surface and how closely it matches the intended design, as shown in Fig. 16. In order to quantitatively evaluate the overall profile error, the mean profile error is calculated based on all machined area point cloud data and the theoretical profile. Results of mean profile errors are included in Table X, with all samples having mean profile errors within ± 0.3 mm, meeting the machining requirements. The actual contour machining accuracy in the processing experiment is higher than the system calibration accuracy. This is because profile tolerance mainly refers to the deviation between the machined contour shape and the theoretical contour shape, rather than the positioning error. At the same time, the sensor robot collected the point cloud data of the workpiece and preliminarily positioned the workpiece to be machined before the actual machining process, and then corrected the position of the workpiece using robot simulation software and simulated machining. In practical applications, to further improve the operational accuracy of the dual-robot system, it is recommended to compensate for the errors in various links of the dual-robot system, such as robot joint parameters, tool coordinate systems, etc. The experimental results show that the calibration method proposed in this article can be used to position the workpieces in the dual-robot machining system, especially for complex surface parts. The dual-robot system successfully machined all samples in the experiment, indicating that the dual-robot system has good application prospects. Based on the dual-robot system, a highly flexible measurement and machining system can be established for larger and more complex workpieces, including fuselage sections, leading edge skins, vertical tail skins, and so on.

Authorized licensed use limited to: Shaanxi Normal University. Downloaded on August 06,2024 at 10:57:59 UTC from IEEE Xplore. Restrictions apply.

V. Conclusion

This article proposes a convex optimization model with quadratic form, utilizing Lie algebra representation of $SE(3)$. The Jacobian matrix of the optimization model is explicitly derived based on the Lie derivative of $SE(3)$. The smoothness properties of Lie group $SE(3)$ allow for simultaneous determination of optimal calibration results through iterations. Due to the closure of Lie group $SE(3)$, the calibration results do not require additional orthogonalization. To balance the impact of rotational and translational optimization variables on the calibration results, a weight coefficient is defined based on the norm of the initial calibration results. Additionally, utilizing the two-step vectorization technique, this article presents a dual-robot initial calibration method to estimate optimal weight coefficients and improve iteration efficiency. A series of simulations and actual experiments were carried out to validate the performance of the proposed method. The experimental results demonstrate the method's superior accuracy and stability. Compared to two existing methods, the mean measurement error of certified ceramic spheres has been reduced from 0.9205 and 0.5363 to 0.4381 mm in actual calibration, respectively. Additionally, dual-robot collaborative machining experiments were conducted on aircraft skin and cavity samples to assess the effectiveness of robotic machining following calibration. All the samples are successfully machined by the dual-robot system in the experiment, indicating that the dual-robot system has good application prospects. The proposed method is a widely applicable calibration approach for a dual-robot system and can be extended to various real-life contexts of multirobot machining for large-scale structures, such as milling, grinding, drilling, and so on.

Appendix A
Lie Algebra $se(3)$ and Lie Group $SE(3)$

The set of rigid body motions is a Lie group, the so-called special Euclidean group, typically denoted as $SE(3)$. The real space $SE(3)$ is a 6-D manifold. Thus, Lie group $SE(3)$ can be parameterized with a twist of dimensions 6×1 called Lie algebra $se(3)$

$$\boldsymbol{\xi} = \begin{bmatrix} \boldsymbol{\rho}^{\mathrm{T}} & \boldsymbol{\phi}^{\mathrm{T}} \end{bmatrix}^{\mathrm{T}} \in se\left(3\right) \tag{64}$$

where the vectors $\boldsymbol{\rho}$ and $\boldsymbol{\phi}$ of dimensions 3×1 correspond to the translational component and rotational component, respectively. Moreover, the set of rotations in the 3-D space is also a Lie group, the so-called special orthogonal group $SO(3)$. Lie algebra $se(3)$ also can be expressed as matrix form, and the operator "$\wedge$" for $se(3)$is defined as follows:

$$\hat{\boldsymbol{\xi}} = \begin{bmatrix} \hat{\boldsymbol{\phi}} & \boldsymbol{\rho} \\ \mathbf{0}^{\mathrm{T}} & 0 \end{bmatrix} \in se\left(3\right) \tag{65}$$

where $\hat{\boldsymbol{\phi}} \in so(3)$ is the skew-symmetric matrix of $\boldsymbol{\phi} \in so(3)$. Exponential map operator $\exp(\boldsymbol{.})$ represents a mapping relationship between Lie algebra and Lie group

$$\boldsymbol{T} = \begin{bmatrix} \boldsymbol{R} & \boldsymbol{t} \\ \mathbf{0}^{\mathrm{T}} & 1 \end{bmatrix} = \exp\left(\hat{\boldsymbol{\xi}}\right) \in SE\left(3\right) \tag{66}$$

$$\boldsymbol{R} = \exp\left(\hat{\boldsymbol{\phi}}\right) \in SO\left(3\right). \tag{67}$$

The exponential map for $SO(3)$ and $so(3)$

$$\begin{aligned} \exp\left(\hat{\boldsymbol{\phi}}\right) &= \exp\left(\phi\hat{\boldsymbol{a}}\right) \\ &= \cos\phi\boldsymbol{I} + \left(1-\cos\phi\right)\boldsymbol{a}\boldsymbol{a}^{\mathrm{T}} + \sin\phi\hat{\boldsymbol{a}} \end{aligned} \tag{68}$$

where ϕ and $\boldsymbol{a}$ for a rotation can be obtained as follows:

$$\phi = \arccos\frac{tr\left(\boldsymbol{R}\right)-1}{2} \tag{69}$$

$$\hat{\boldsymbol{a}} = \frac{1}{\sin\phi}\left(\boldsymbol{R}-\boldsymbol{R}^{\mathrm{T}}\right). \tag{70}$$

The exponential map for $SE(3)$ and $se(3)$

$$\exp\left(\hat{\boldsymbol{\xi}}\right) = \begin{bmatrix} \exp\left(\hat{\boldsymbol{\phi}}\right) & \boldsymbol{J}\boldsymbol{\rho} \\ \mathbf{0}^{\mathrm{T}} & 1 \end{bmatrix} \tag{71}$$

where $\boldsymbol{J} = \frac{\sin\phi}{\phi}\boldsymbol{I} + (1-\frac{\sin\phi}{\phi})\boldsymbol{a}\boldsymbol{a}^{\mathrm{T}} + \frac{1-\cos\phi}{\phi}\hat{\boldsymbol{a}}$. The exponential map for $SO(3)$ is also known as Rodrigues formulas.

Appendix B
Adjoint Transformation of Lie Group $SE(3)$ and Lie Algebra $se(3)$

In Lie theory, adjoint transformation is a linear transformation, and can transform a tangent vector from the tangent space around one element to the tangent space of another. For a rigid transformation $\boldsymbol{T} \in SE(3)$, adjoint transformation is denoted as $Ad(\boldsymbol{.})$and defined as follows:

$$Ad\left(\boldsymbol{T}\right) = Ad\left(\begin{bmatrix} \boldsymbol{R} & \boldsymbol{t} \\ \mathbf{0}^{\mathrm{T}} & 1 \end{bmatrix}\right) = \begin{bmatrix} \boldsymbol{R} & \hat{\boldsymbol{t}}\boldsymbol{R} \\ \mathbf{0} & \boldsymbol{R} \end{bmatrix} \tag{72}$$

where $\boldsymbol{R}$ is the corresponding rotational component of the rigid transformation, $\boldsymbol{t}$ is the corresponding translational component of the rigid transformation, and $\hat{\boldsymbol{t}}$ is the skew-symmetric matrix of the translational component. For a twist $\boldsymbol{\xi} \in se(3)$, adjoint transformation is denoted as $ad(\boldsymbol{.})$ and defined as follows:

$$ad\left(\hat{\boldsymbol{\xi}}\right) = \boldsymbol{\xi}^{\curlywedge} = \begin{bmatrix} \boldsymbol{\rho} \\ \boldsymbol{\phi} \end{bmatrix}^{\curlywedge} = \begin{bmatrix} \hat{\boldsymbol{\phi}} & \hat{\boldsymbol{\rho}} \\ \mathbf{0} & \hat{\boldsymbol{\phi}} \end{bmatrix} \tag{73}$$

where operator "$\curlywedge$" also represents adjoint transformation of a twist, and $\hat{\boldsymbol{\phi}}$ and $\hat{\boldsymbol{\rho}}$ are the corresponding skew-symmetric matrix of the vectors $\boldsymbol{\rho}$ and $\boldsymbol{\phi}$, respectively.

In addition, the map from $Ad(\boldsymbol{T})$ to $\exp(ad(\boldsymbol{\xi}^{\wedge}))$ is also defined by exponential map

$$\begin{aligned} Ad\left(\hat{\boldsymbol{\xi}}\right) &= \exp\left(ad\left(\boldsymbol{\xi}^{\wedge}\right)\right) \\ &= \begin{bmatrix} \exp\left(\boldsymbol{\phi}^{\wedge}\right) & \left(\boldsymbol{J}\boldsymbol{\rho}\right)^{\wedge}\exp\left(\boldsymbol{\phi}^{\wedge}\right) \\ \mathbf{0} & \exp\left(\boldsymbol{\phi}^{\wedge}\right) \end{bmatrix}. \end{aligned} \tag{74}$$

References

[1] A. Khamis, A. Hussein, and A. Elmogy, "Multi-robot task allocation: A review of the state-of-the-art," in *Cooperative Robots and Sensor Networks*. Berlin, Germany: Springer, 2015, pp. 31–51.

[2] D. Zhu et al., "Robotic grinding of complex components: A step towards efficient and intelligent machining – challenges, solutions, and applications," *Robot. Comput.-Integr. Manuf.*, vol. 65, 2020, Art. no. 101908.

Authorized licensed use limited to: Shaanxi Normal University. Downloaded on August 06,2024 at 10:57:59 UTC from IEEE Xplore. Restrictions apply.

[3] G. Wang, W.-L. Li, C. Jiang, and H. Ding, "Machining allowance calculation for robotic edge milling an aircraft skin considering the deformation of assembly process," *IEEE/ASME Trans. Mechatron.*, vol. 27, no. 5, pp. 3350–3361, Oct. 2022.
[4] R. Bogue, "The growing use of robots by the aerospace industry," *Ind. Robot.*, vol. 45, no. 6, pp. 705–709, 2018.
[5] Airbus, *Airbus Inaugurates New A320 Structure Assembly Line in Hamburg*, 2019. [Online]. Available: https://www.airbus.com/en/newsroom/press-releases/2019-10-airbus-inaugurates-new-a320-structure-assembly-line-in-hamburg
[6] Fraunhofer IFAM, *JEC WORLD – Sustainable and efficient production through automation and robotics from Fraunhofer IFAM in Stade, Germany*, 2023. [Online]. Available: https://www.ifam.fraunhofer.de/en/Press_Releases/sustainable-and-efficient-production-through-automation-and-robotics.html
[7] P. Koch, P. Rawal, N. Töpfer, T. Haß, C. Böhlmann, and W. Hintze, "Modular lightweight robot system for aircraft production using a generic OPC UA skill concept," *Prod. Eng.*, vol. 17, no. 2, pp. 329–339, 2023.
[8] Y. C. Shiu and S. Ahmad, "Calibration of wrist-mounted robotic sensors by solving homogeneous transform equations of the form AX = XB," *IEEE Trans. Robot. Automat.*, vol. 5, no. 1, pp. 16–29, Feb. 1989.
[9] R. Y. Tsai and R. K. Lenz, "A new technique for fully autonomous and efficient 3D robotics hand/eye calibration," *IEEE Trans. Robot. Automat.*, vol. 5, no. 3, pp. 345–358, Jun. 1989.
[10] J. C. K. Chou and M. Kamel, "Finding the position and orientation of a sensor on a robot manipulator using quaternions," *Int. J. Robot. Res.*, vol. 10, no. 3, pp. 240–254, 1991.
[11] F. C. Park and B. J. Martin, "Robot sensor calibration: Solving AX = XB on the Euclidean group," *IEEE Trans. Robot. Automat.*, vol. 10, no. 5, pp. 717–721, Oct. 1994.
[12] N. Andreff, R. Horaud, and B. Espiau, "Robot hand-eye calibration using structure-from-motion," *Int. J. Robot. Res.*, vol. 20, no. 3, pp. 228–248, 2001.
[13] K. Daniilidis, "Hand-eye calibration using dual quaternions," *Int. J. Robot. Res.*, vol. 18, no. 3, pp. 286–298, 1999.
[14] Z. Zhao, "Hand-eye calibration using convex optimization," in *Proc. IEEE Int. Conf. Robot. Automat.*, 2011, pp. 2947–2952.
[15] J. Heller, M. Havlena, and T. Pajdla, "Globally optimal hand-eye calibration using branch-and-bound," *IEEE Trans. Pattern Anal. Mach. Intell.*, vol. 38, no. 5, pp. 1027–1033, May 2016.
[16] F. Dornaika and R. Horaud, "Simultaneous robot-world and hand-eye calibration," *IEEE Trans. Robot. Automat.*, vol. 14, no. 4, pp. 617–622, Aug. 1998.
[17] M. Shah, "Solving the robot-world/hand-eye calibration problem using the Kronecker product," *J. Mech. Robot.*, vol. 5, no. 3, 2013, Art. no. 031007.
[18] A. G. Li, L. Wang, and D. F. Wu, "Simultaneous robot-world and hand-eye calibration using dual-quaternions and Kronecker product," *Int. J. Robot. Res.*, vol. 5, no. 10, pp. 1530–1536, 2010.
[19] S. Remy, M. Dhome, J. M. Lavest, and N. Daucher, "Hand-eye calibration," in *Proc. IEEE/RSJ Int. Conf. Intell. Robot Syst.. Innov. Robot. Real-World Appl.*, 1997, vol. 2, pp. 1057–1065.
[20] K. H. Strobl and G. Hirzinger, "Optimal hand-eye calibration," in *Proc. IEEE/RSJ Int. Conf. Intell. Robot. Syst.*, 2006, pp. 4647–4653.
[21] F. Ernst et al., "Non-orthogonal tool/flange and robot/world calibration," *Int. J. Med. Robot. Comput. Assist. Surg.*, vol. 8, no. 4, pp. 407–420, 2012.
[22] Z. J. Zhao, "Simultaneous robot-world and hand-eye calibration by the alternative linear programming," *Pattern Recognit. Lett.*, vol. 127, pp. 174–180, 2019.
[23] J. H. Fu, H. D. Liu, M. Q. He, and D. H. Zhu, "A hand-eye calibration algorithm of binocular stereo vision based on multi-pixel 3D geometric centroid relocalization," *J. Adv. Manuf. Sci. Technol.*, vol. 2, no. 1, 2022, Art. no. 2022005.
[24] H. Liu, J. Fu, L. Tian, and D. Zhu, "Convergent binocular vision algorithm for guiding machining robot under extended imaging dynamic range," *Measurement*, vol. 203, 2022, Art. no. 112013.
[25] R. G. Bonitz and T. C. Hsia, "Calibrating a multi-manipulator robotic system," *IEEE Robot. Automat. Mag.*, vol. 4, no. 1, pp. 18–22, Mar. 1997.
[26] Y. Qiao, Y. P. Chen, B. Chen, and J. M. Xie, "A novel calibration method for multi-robots system utilizing calibration model without nominal kinematic parameters," *Precis. Eng.-J. Int. Soc. Precis. Eng. Nanotechnol.*, vol. 50, pp. 211–221, 2017.
[27] D. Zhao, Y. B. Bi, and Y. L. Ke, "Kinematic modeling and base frame calibration of a dual-machine-based drilling and riveting system for aircraft panel assembly," *Int. J. Adv. Manuf. Technol.*, vol. 94, no. 5-8, pp. 1873–1884, 2018.
[28] Q. Zhu, X. Xie, and C. Li, "Dual manipulator system calibration based on virtual constraints," *Bull. Polish Acad. Sci., Tech. Sci.*, vol. 67, no. 6, pp. 1149–1159, 2019.
[29] Q. Zhu, X. Xie, C. Li, G. Xia, and Q. Liu, "Kinematic self-calibration method for dual-manipulators based on optical axis constraint," *IEEE Access*, vol. 7, pp. 7768–7782, 2019.
[30] C. Ruan, X. Gu, Y. Li, G. Zhang, W. Wang, and Z. Hou, "Base frame calibration for multi-robot cooperative grinding station by binocular vision," in *Proc. IEEE 2nd Int. Conf. Robot. Automat. Eng.*, 2017, pp. 115–120.
[31] J. Wang, W. Wang, C.-H. Wu, S.-L. Chen, J.-H. Fu, and G.-D. Lu, "A plane projection based method for base frame calibration of cooperative manipulators," *IEEE Trans. Ind. Inform.*, vol. 15, no. 3, pp. 1688–1697, Mar. 2019.
[32] S. J. Yan, S. K. Ong, and A. Y. C. Nee, "Registration of a hybrid robot using the degradation-Kronecker method and a purely nonlinear method," *Robotica*, vol. 34, no. 12, pp. 2729–2740, 2016.
[33] Z. Fu, J. Pan, E. Spyrakos-Papastavridis, X. Chen, and M. Li, "A dual quaternion-based approach for coordinate calibration of dual robots in collaborative motion," *IEEE Robot. Automat. Lett.*, vol. 5, no. 3, pp. 4086–4093, Jul. 2020.
[34] L. Wu, J. Wang, L. Qi, K. Wu, H. Ren, and M. Q.-H. Meng, "Simultaneous hand-eye, tool-flange, and robot-robot calibration for comanipulation by solving the AXB = YCZ problem," *IEEE Trans. Robot.*, vol. 32, no. 2, pp. 413–428, Apr. 2016.
[35] J. Wang, L. Wu, M. Q.-H. Meng, and H. Ren, "Towards simultaneous coordinate calibrations for cooperative multiple robots," in *Proc. IEEE/RSJ Int. Conf. Intell. Robot. Syst.*, 2014, pp. 410–415.
[36] Q. Ma, Z. Goh, S. Ruan, and G. S. Chirikjian, "Probabilistic approaches to the AXB = YCZ calibration problem in multi-robot systems," *Auton. Robot.*, vol. 42, no. 7, pp. 1497–1520, 2018.
[37] G. Wang et al., "Simultaneous calibration of multicoordinates for a dual-robot system by solving the AXB = YCZ problem," *IEEE Trans. Robot.*, vol. 37, no. 4, pp. 1172–1185, Aug. 2021.
[38] J. Jiang, X. Luo, S. Xu, Q. Luo, and M. Li, "Hand-eye calibration of EOD robot by solving the AXB = YCZD problem," *IEEE Access*, vol. 10, pp. 3415–3429, 2022.
[39] Y. Qin, P. Geng, B. Lv, Y. Meng, Z. Song, and J. Han, "Simultaneous calibration of the hand-eye, flange-tool and robot-robot relationship in dual-robot collaboration systems," *Sensors*, vol. 22, no. 5, 2022, Art. no. 1861.
[40] H. Xie, C. T. Pang, W. L. Li, Y. H. Li, and Z. P. Yin, "Hand-eye calibration and its accuracy analysis in robotic grinding," in *Proc. IEEE Int. Conf. Automat. Sci. Eng.*, 2015, pp. 862–867.

Cheng Jiang received the B.E. degree in mechanical design, manufacturing and automation in 2016 from the Huazhong University of Science & Technology, Wuhan, China, where he is currently working toward the doctoral degree in mechanical engineering.

His research interests include point cloud processing and robot machining.

Wen-long Li (Member, IEEE) received the B.E. degree in mechanical engineering and automation from Xi'an Jiaotong University, Xi'an, China, in 2004, and the Ph.D. degree in mechatronic engineering from the Huazhong University of Science and Technology (HUST), Wuhan, China, in 2010.

He is currently a Professor with HUST. His current research interests include robotic machining and 3-D optical measurement.

Authorized licensed use limited to: Shaanxi Normal University. Downloaded on August 06,2024 at 10:57:59 UTC from IEEE Xplore. Restrictions apply.

Wen-pan Li received the B.E. degree in mechanical design, manufacturing and automation from the Northwestern University of Agricultural and Forestry Science and Technology, Xianyang, China, in 2015, and the Ph.D. degree in mechanical engineering from the City University of Hong Kong, Hong Kong, in 2022.

He is currently carrying out the postdoctoral research in mechanical engineering with the City University of Hong Kong. His research interests include visual inspection of 3-D profile and optical measurement technology.

Dong-fang Wang received the B.E. degree in mechanical design, manufacturing, and automation from the Wuhan University of Technology, Wuhan, China, in 2020. He is currently working toward the doctoral degree in mechanical engineering with the Huazhong University of Science and Technology, Wuhan.

His research interests include robot measurement and machining.

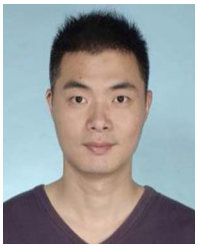

Li-jun Zhu received the B.E. degree in mechanical manufacturing and automation from Xi'an Jiaotong University, Xi'an, China, in 2006, the M.Eng. degree in mechatronic engineering from the Huazhong University of Science and Technology (HUST), Wuhan, China, in 2008, and the Ph.D. degree in control science and engineering from the University of Newcastle, Callaghan, NSW, Australia, in 2013.

From 2015 to 2018, he was a Postdoctoral Researcher with the University of Hong Kong, Hong Kong. He is currently a Professor with HUST. His research interests include networked control and intelligent control of robot.

Wei Xu received the B.E. degree in energy power engineering and the M. Eng. degree in fluid machinery and engineering from the China University of Mining and Technology, Xuzhou, China, in 2013 and 2016, respectively, and the Ph.D. degree in measurement engineering from Leibniz University Hannover, Hannover, Germany, in 2021.

He is currently carrying out the postdoctoral research in mechanical engineering with the Huazhong University of Science and Technology, Wuhan, China. His research interests include the application of vision measurement and deep learning in robotic machining.

Huan Zhao received the B.S. degree in mechanical engineering from Jilin University, Changchun, China, in 2006, and the Ph.D. degree in mechanical engineering from Shanghai Jiao Tong University, Shanghai, China, in 2013.

From 2013 to 2015, he was a Postdoctoral Researcher with the Huazhong University of Science and Technology (HUST), Wuhan, China. He is currently a Professor with HUST. His research interests include force control, visual servoing, and machine learning with applications to robotic machining.

Han Ding (Member, IEEE) received the Ph.D. degree in mechanical engineering from the Huazhong University of Science and Technology (HUST), Wuhan, China, in 1989.

Supported by the Alexander von Humboldt Foundation, he was a Researcher with the University of Stuttgart, Stuttgart, Germany, from 1993 to 1994. He has been a Professor with HUST since 1997. He was a "Cheung Kong" Chair Professor of Shanghai Jiao Tong University from 2001 to 2006. His research interests include intelligent manufacturing and robotics machining.

Dr. Diang was elected a member of the Chinese Academy of Sciences in 2013.

Authorized licensed use limited to: Shaanxi Normal University. Downloaded on August 06,2024 at 10:57:59 UTC from IEEE Xplore. Restrictions apply.